



Catalytic and kinetic evaluation of Fe/HZSM-5 catalyst for Fischer-Tropsch synthesis

Lucas Alves da Silva^a, Vilma Heczko^b, Martin Schmal^a, Pedro Henrique Cury Camargo^b, Rita Maria Brito Alves^{a,*}, Reinaldo Giudici^{a,*}

^a Universidade de São Paulo, Escola Politécnica, Department of Chemical Engineering, Avenida Professor Luciano Gualberto, 380 Travessa 3, CEP 05508-010 São Paulo, SP, Brasil

^b UH: University of Helsinki, Department of Chemistry, A. I. Virtasen aukio 1, Helsinki, Finland

ARTICLE INFO

Keywords:

CO hydrogenation
Zeolites
Iron
Kinetics
Hydrocarbons

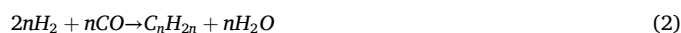
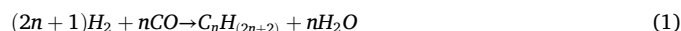
ABSTRACT

Rising global energy and growing environmental concerns demand cleaner production methods for fuels and platform chemicals. The Fischer-Tropsch synthesis (FTS) is a promising alternative to fossil oil sources for producing valuable hydrocarbons directly from syngas (CO and H₂) such as light olefins and middle distillates. Due to their cost-effectiveness and bifunctional properties, Fe/HZSM-5 catalysts have gained recent interest for FTS. However, research on reaction conditions and CO consumption kinetics for this catalyst remains limited. This work addresses a comprehensive study encompassing catalyst characterization, catalytic activity evaluation, and kinetic modeling of Fe/HZSM-5 catalysts for FTS. Our data showed that Fe presented multiple reduction stages and changed the moderate acidity of the evaluated zeolites upon Fe impregnation. Fe₂O₃ particles were also found to be transformed into iron carbides species during the catalytic reaction according to the Mössbauer spectroscopy. The catalysts were active and stable for FTS (X_{CO} > 50 %) with a major production of hydrocarbons in C₂-C₄ and C₅-C₈ ranges. Pressure, temperature, feed composition and space velocity significantly influenced the CO conversion. The kinetic model for the Fe/HZSM-5 catalyst was investigated by modeling and in situ DRIFTS, aligning with the carbide mechanism considering dissociative adsorption of CO and H₂, a two-site reaction pathway, and competitive adsorption between CO and CO₂ on the metal sites. These findings provide important insights for optimizing catalyst design and reaction conditions to enhance the efficiency of syngas-based fuel production.

1. Introduction

The world's growing energy demand, coupled with the urgency of addressing climate change, requires a rapid shift towards sustainable energy sources. As the International Energy Agency (IEA)'s 2023 World Energy report emphasizes [1], clean energy investment is on the rise, (40 % since 2020). Nevertheless, fossil fuels remain a dominant part of the global energy mix followed by coal and natural gas [2]. Technologies of carbon capture and utilization (CCU), such as CO₂ conversion to valuable hydrocarbons, offer a critical path to reduce reliance on fossil fuels and greenhouse gas emissions [3]. The Fischer-Tropsch synthesis (FTS) thus represents a core component of gas-to-liquid (GTL) processes that transform syngas (CO + H₂) into synthetic hydrocarbons and valuable chemicals [4]. FTS comprises a series of reactions (Eq. (1) and Eq. (2)) involving a polymerization-like mechanism in which syngas is

converted to hydrocarbons [5] according to the Anderson-Schulz-Flory (ASF) distribution model. Competing side reactions, such as methanation (Eq. (3)) and water-gas-shift (WGS) (Eq. (4)), make it very challenging to control reaction selectivity in FTS [6].



Effective FTS catalysts require metals capable of adsorbing CO and H₂. Commercial processes commonly use iron (Fe), or cobalt (Co)-based catalysts [7–9]. According to the literature, ruthenium (Ru) is one of the

* Corresponding authors.

E-mail addresses: rmbalves@usp.br (R.M. Brito Alves), rgiudici@usp.br (R. Giudici).

most active metals for FTS at low temperatures; however, it remains an expensive metal. Nickel (Ni) is active for FTS; however, it exhibits high methanation activity. Therefore, the current state of catalyst design is focused on the development of Fe and Co-based catalysts, which show activity for FTS and a better cost-benefit ratio [10]. Various Fe or Co-based FTS catalysts supported on alumina, silica, metal oxides, carbon materials, or structured materials (e.g., MOFs, zeolites) have been reported [11–13]. Co-based catalysts exhibit higher stability and selectivity toward long-chain hydrocarbons compared to Fe-based catalysts, despite being more sensitive to variations in operating conditions [10]. Studies on Co-based catalyst design explore the influence of particle size and exposed crystal faces [14]. Metallic crystalline forms such as α -Co (hcp) and β -Co (fcc) are active sites for CO conversion [4]. Co carbides such as Co_2C and Co_3C have also been studied as active phases in FTS [15]. On the other hand, iron-based catalysts are known for operating under flexible conditions, and studies have been conducted with various supports for these catalysts in order to improve their stability. Fe catalysts undergo reduction before FTS, converting hematite (Fe_2O_3) to magnetite (Fe_3O_4), FeO, or metallic iron (Fe). The reduced species can be transformed into iron carbides, which are the active sites for hydrocarbon chain growth. Jun et al. [16] compared SiO_2 and Al_2O_3 supports for Fe-K-Cu catalysts in FTS. Al_2O_3 improved metals distribution compared to SiO_2 , leading to higher carbide content and middle distillate selectivity (21 % vs. 9 %). Similar trends were observed by Lu et al. [11], who reported the influence of these supports on the electronic state of Fe particles, which influence the formation of C-rich iron carbide species. Mesoporous materials have also been studied as potential supports for FTS. Cheng et al. [12] investigated MCM-41 as Fe catalyst support on FTS. According to the study, the performance of Fe catalysts depended on the degree of reduction and carbidization of the metallic particles. Higher dispersion of iron oxide on smaller pore mesoporous silicas led to poorer CO hydrogenation (X_{CO} : 19 %) whereas the mesoporous support exhibited superior catalytic performance (X_{CO} : 33 %). The effect of particle size using mesoporous support was also investigated using Co supported on MCM-41 by Khodakov et al. [17] and on SBA-15 by Xiong et al. [18]. Carbon-based materials, including reduced graphene oxide (rGO), carbon nanofibers (CNFs) and carbon nanotubes (CNTs) have also been studied as supports for FTS. Valero-Romero et al. [13] and Chen et al. [19] observed enhanced Fe reduction and carbidization in carbon-based supports due to the support chemical composition and low metal-support interaction. Similarly, Chen et al. [19] and Yu et al. [20] observed enhanced iron carbide formation in Fe-carbon confined materials, promoting C_{5+} selectivity. Promoted-metal catalysts have also been reported to improve CO hydrogenation and liquid products selectivity [21]. Alkali promoters, particularly K, are known to facilitate the formation of iron carbides, increasing C_{5+} selectivity [22–24]. Among the different supports studied, zeolites are promising as metal/zeolite systems are bifunctional, presenting metal sites for chain growth as well as tunable acidic sites for secondary reactions, such as cracking and isomerization [25]. HZSM-5 zeolites show potential as support over other zeolite types due to their established industrial use in different processes, high stability under FTS conditions, and oligomerization capacity of formed chains [26,27]. Fe catalyst performance in FTS depends on factors such as the active iron oxide (Fe_2O_3 , Fe_3O_4 , FeO) and carbide (γ - Fe_5C_2 , θ - Fe_3C , Fe_7C_3) phases, the quantity and strength of acid sites, and the material porosity [25]. In terms of active phase, carbides represent the most active species for chain growth in FTS reactions and are formed by nucleation as small nodules on the surface of iron oxides upon exposure to CO [28]. In terms of acidity, it has been established that a balance between the quantity and strength of acid sites in zeolites is crucial for the selective production of hydrocarbons. Increasing the number of acid sites in Fe/H-ZSM-5 catalysts has been reported to decrease the selectivity of heavy C_{13+} hydrocarbons due to the over cracking of longer chains [29,30]. Concerning the porous structure of zeolites, it has been shown that long micropores enhance the diffusional resistance of hydrocarbons, facilitating the cracking effect

[25]. Peng et al. [31] demonstrated effective control of long-chain hydrocarbon selectivity in FTS using a mesoporous Co/zeolite Y catalyst. Similar results were observed by Cheng et al. [32] with Fe/H-ZSM-5 catalysts, in which the zeolite pore sizes influenced the selectivity to C_5 – C_8 (gasoline range) hydrocarbons. Finally, the synthesis method strongly affects metal dispersion and, consequently, catalytic performance [33,34].

Despite reported research on metal/zeolite FTS catalysts, a comprehensive understanding of Fe/HZSM-5 remains limited in terms of correlating catalyst physicochemical properties and reaction condition optimization as well as reaction kinetics of CO conversion. Kinetic modeling of FTS is complex due to the nature of the reactions involved and byproducts formed.

There is no consensus on whether secondary molecules formed in FTS, such as H_2O and CO_2 , influence the reaction rate [35,36]. The kinetic modeling studies for FTS catalysts are limited in the literature, mostly focusing on models developed for fused or precipitated Fe catalysts. Challenges are presented around acquiring experimental data and dealing with the gas–liquid complexity of the FTS reactions. Few studies of kinetics have been conducted with supported catalysts so far, and to our knowledge, none have been carried out for an iron catalyst supported on HZSM-5. Developing a reaction rate model for Fe/H-ZSM-5 is crucial for optimizing the performance of this catalyst both experimentally and for designing and numerically simulating industrial-scale processes.

For addressing this challenge, a comprehensive investigation was performed on Fe/HZSM-5 catalysts for FTS encompassing synthesis, *ex situ* and *in situ* characterization, evaluation and optimization of reaction conditions, and kinetic modeling. This strategy enabled the elucidation of mechanistic insights and the determination of the kinetic parameters for this catalyst in FTS, which was the motivation of the present work. The data showed that the catalysts were active and stable for FTS ($X_{\text{CO}} > 50\%$) with a major production of hydrocarbons in the C_2 – C_4 and C_5 – C_8 ranges. Operating conditions, such as pressure, temperature, feed composition and space velocity significantly influenced the CO conversion. Fe presented multiple reduction stages and an alteration in the moderate acidity of the evaluated zeolites upon Fe impregnation. Fe_2O_3 transformed into Fe_5C_2 carbides under reaction conditions. The proposed kinetic model aligns with the carbide mechanism considering dissociative adsorption of CO and H_2 , a two-site reaction pathway, and competitive adsorption between CO and CO_2 on the metal sites.

2. Experimental

The present work comprises two complementary studies: the first part is concentrated on investigating Fe-zeolite catalysts through characterization and conventional catalytic tests, evaluating the influence of reaction conditions including pressure, temperature, space velocity, and feed composition on FTS. The second part focused on conducting a kinetic study of the CO hydrogenation reaction over the Fe/zeolite catalyst, in which reaction kinetic data were experimentally obtained and studied using reaction rate models.

2.1. Catalyst preparation

Initially, Fe_3O_4 nanoparticles (NPs) were synthesized via precipitation as reported by Wei et al. [37] and subsequently, impregnated on the zeolite support, using the dry impregnation method. Three commercial HZSM-5 zeolites of different $\text{SiO}_2/\text{Al}_2\text{O}_3$ (52, 91 and 371) were purchased from ACS Material® with high purity ($\geq 98\%$). Zeolites of different compositions were chosen for the present study in order to evaluate the possible effects of acidic, basic, and metallic sites on the performance of the catalysts for CO hydrogenation. First, the Fe_3O_4 NPs were prepared by dissolving 0.501 g of $\text{FeCl}_2 \cdot 4\text{H}_2\text{O}$ and 1.262 g of $\text{FeCl}_3 \cdot 6\text{H}_2\text{O}$ in 6.0 mL of deionized water with 0.2 mL of HCl (37 %). The solution was stirred at 60 °C, and 16.0 mL of NaOH (37 %) was added

dropwise. After 1 h, the black mixture was cooled, and the particles were separated, washed, and dried at 60 °C. The resulting particles were ground before the impregnation step. The nanoparticles of Fe₃O₄ were suspended in deionized water (50 mg/mL), and a portion of this solution was mixed with the zeolite until a slurry was formed. The mixture was dried at 60 °C for 25 min. This process continued until all the suspension had been utilized. Then, the sample underwent grinding in an agate mortar and calcination at 550 °C for 4 h under airflow. All catalysts were prepared with a Fe₃O₄/HZSM-5 mass ratio of 1, resulting in a theoretical Fe loading of 36 % wt. The synthesized catalysts were named Fe-Z52DI, Fe-Z91DI and Fe-Z371DI. Here, Z52, Z91, and Z371 refer to the different SiO₂/Al₂O₃ and DI to the dry impregnation method for synthesizing the catalysts, as shown in Table 1.

2.2. Catalyst characterization

Thermogravimetric analysis (TGA) was conducted on a Shimadzu thermobalance DTG-60H under heating and synthetic air flow (100 mL/min, 30 °C/min 25–1000 °C).

Fourier Transformed Infrared spectroscopy (FTIR) was performed on a Shimadzu spectrophotometer IRPrestige-21 with 45 scans (400–4000 cm⁻¹) using the Attenuated Total Reflectance (ATR) technique. The pure solid samples were placed on the reflectance crystal module and the analyses were conducted under atmospheric conditions.

Raman spectroscopy was carried out on a Renishaw InVia Raman microscope equipped with argon laser (50 mW) of wavelength $\lambda = 532$ nm in the range of 100–2200 cm⁻¹.

X-ray diffraction (XRD) was performed on a Rigaku MiniFlex diffractometer with CuK α radiation at 30 kV, 10 mA (8–80° 2 θ Bragg angle) with a 0.02 step width and 0.5 s counting time.

Textural properties were evaluated with N₂ physisorption isotherms carried out on a Micromeritics ASAP-2020. The samples were degassed under vacuum (120 °C for 12 h) and the analysis was conducted at N₂ boiling point (77 K).

Transmission Electron Microscopy (TEM) images were taken on a JEOL JEM 2100 microscope. Prior to the analysis, the samples were dispersed in ethanol and ultrasonicated for 15 min.

Temperature programmed reduction (TPR) and temperature programmed desorption (TPD) analyses were conducted on an Autochem II 2920-Micromeritics. For TPR, samples were pre-degassed at 150 °C for 30 min under air flow, followed by analysis under H₂/Ar (10 vol%) flow from 30 to 900 °C (10 °C/min). TPD curves using CO, CO₂, and NH₃ as probe molecules were obtained to assess basic and acid sites, and CO adsorption capacity. The samples were degassed under air flow at 150 °C for 30 min, followed by reduction at 450 °C (10 °C/min) under H₂/Ar (10 % vol.). Subsequently, the samples were set under flux of NH₃, CO₂, or CO (10–15 vol%) for 1 h. Then, the system was purged with pure He for 1 h in order to avoid residual gases in the system or those physically adsorbed. The desorption temperature ramp occurred from 30 to 900 °C (10 °C·min⁻¹).

A CO pulse chemisorption analysis was performed to determine the metallic surface area and subsequently calculate the Turnover Frequency (TOF) parameter for CO consumption. The analysis was conducted on an Autochem II 2920-Micromeritics. The sample was pre-degassed at 150 °C for 30 min under airflow, followed by reduction under a H₂/Ar (10 %) flow at 450 °C (10 °C/min). After reduction, the sample was cooled to 30 °C. Subsequently, 10 pulses of 3.5x10⁻² cm³ of CO were applied to the sample.

Table 1
Catalysts identification.

Catalyst	SiO ₂ /Al ₂ O ₃	Synthesis method
Fe-Z52DI	52	Dry impregnation
Fe-Z91DI	91	Dry impregnation
Fe-Z371DI	371	Dry impregnation

Diffuse Reflectance Infrared Fourier Transform Spectroscopy *in situ* (DRIFTS) was conducted on a Shimadzu spectrophotometer IRPrestige-21 to assess adsorbed molecules under FTS reaction environment. The catalyst was first reduced *in situ* using H₂ flow (WHSV of 4800 mL.g⁻¹.h⁻¹) at 450 °C for 1 h. Next, the catalyst underwent continuous flow of CO/H₂/N₂ (3:6:1), with a WHSV of 4000 mL.g⁻¹.h⁻¹ at 8 bar. The spectra were obtained at temperatures of 260, 280, 300, and 320 °C with a resolution of 4 cm⁻¹ between 4000 and 700 cm⁻¹.

Content of Fe was analyzed by Microwave-Assisted Plasma Atomic Emission spectrometry (MP AES, Agilent technologies 4200). Triplicate samples were digested in hydrochloric acid and spectral lines at 371.993 nm and 373.486 nm were analyzed relative to calibration curve.

⁵⁷Fe Mössbauer spectroscopy experiments were carried out on a WissEl spectrometer (Starnberg, Germany) at room temperature. The analysis was conducted in transmission geometry with the samples and the ⁵⁷Co:Rh matrix source moving sinusoidally. The hyperfine parameter isomer shift (IS) values were expressed relative to metallic iron.

2.3. Fischer-Tropsch catalyst test

Catalytic experiments were performed using a GTL Microactivity Effi automated reactor setup by PID Eng&Tech – Micromeritics®, which regulated flow rate, temperature, and pressure. The system featured both hot (190 °C) and cold (5 °C) trap condensers along with an external heating line. The resulting products were examined using a chromatograph (Shimadzu® GC-2010 Plus) equipped with a flame ionization detector (FID) and a thermal conductivity detector (TCD). A fixed-bed Hastelloy C reactor, ID of 9.1 mm, was set up with quartz wool and filled with catalyst, varying from 100 to 200 mg based on the target Weight Hourly Space Velocity (WHSV). The bed volume was maintained at up to 1 cm³ with the aid of glass microspheres when necessary. The catalyst underwent *in-situ* pre-reduction with pure H₂ (WHSV of 4800 mL.g⁻¹.h⁻¹) at 450 °C for 4 h. The system was then cooled to the reaction temperature, switched to reaction gases feed flow (H₂:CO:N₂ 15.0:7.5:2.2 mL.min⁻¹) and increased pressure to 20 bar. Initially, tests were carried out with the Fe-Z91DI catalyst by increasing the temperature *in situ* according to: 260 °C → 300 °C → 350 °C → 300 °C. Afterwards, all catalysts were evaluated under similar conditions, and for the best performing catalyst, the effect of temperature (260, 280, 300 and 320 °C), WHSV (4000, 6880, and 9000 mL.g⁻¹.h⁻¹), pressure (1, 10, 20, and 20 bar), and H₂/CO feed (1.0, 1.5, and 2.0) was investigated. Finally, a long stability test was performed for 72 h with time on stream (TOS). The CO conversion, CO₂ selectivity, and hydrocarbon selectivity were calculated based on chromatographic analysis, as detailed in the [Supplementary material](#).

2.4. Fischer-Tropsch kinetic assessment

The experiments for kinetic assessment were carried out in the same reaction system described previously. Prior to collecting kinetic data, the reaction kinetic regime was assessed based on X_{CO} vs W/F curve, where W is catalyst mass and F is the gas space velocity. Then, the Mears and Weisz-Prater criteria for external and internal diffusion were estimated (see [Supplementary material](#)). The catalyst reduction was set with pure H₂ (WHSV of 4800 mL.g⁻¹.h⁻¹) for 4 h at 450 °C. The experimental tests for kinetic data collection were carried out at WHSV of 160000 mL.g⁻¹.h⁻¹ at 20 bar, for different temperatures- (260, 280, 300, and 310 °C) and H₂/CO molar feed ratio (1.0, 1.5, 2.0, and 3.0). Then, the CO consumption rate was obtained by Eq. (5) considering a differential reactor, as previously reported [35].

$$-r_{CO}' = \frac{F_{CO}^{inlet} X_{CO}}{W_{cat}} \quad (5)$$

where F_{CO}^{inlet} is the CO molar inlet flow, X_{CO} is the CO conversion and W_{cat}

is the catalyst mass.

Based on the literature, different LHHW models were chosen using experimental data of the Fe-Z91DI catalyst, determining the reaction rates according to Eq. (6):

$$-r'_{co} = f(T, pH_2, pCO, pCO_2, pH_2O) \quad (6)$$

Then, the kinetic models were adjusted with the experimental data using a nonlinear regression and the Levenberg-Marquardt algorithm. The codes were implemented in Python programming language. To assess the quality of the fit, calculations were performed for the coefficient of determination, Root Mean Square Error (RMSE), and Fisher-Snedecor test (F Value).

3. Results and discussion

This section presents the results, which were organized into three subsections: catalyst characterizations, Fischer-Tropsch catalytic activity, and Fischer-Tropsch kinetic assessment.

3.1. Catalyst characterizations

The catalyst characterization studies were focused on the analyzes related to the structure of the material and the present sites on the catalyst surface.

3.1.1. Structures

The thermogravimetric profiles of the catalysts (Fig. S1) presented low mass losses (<10 %), indicating the thermal stability of prepared samples. FTIR and Raman spectroscopies results are shown in Fig. 1a and b for identifying Si-O-Al and Fe-O bonds vibration, respectively. The FTIR spectra (Fig. 1a) exhibited typical bands of aluminosilicate within the 400–1300 cm^{-1} range, indicating that Fe deposition did not change the zeolite structure. The bands at 550 cm^{-1} and 1230 cm^{-1} denoted external stretching of 5-membered ring blocks, which are

characteristic structures of the HZSM-5 zeolite. Other bands at 800 cm^{-1} , 450 cm^{-1} , and 1100 cm^{-1} are attributed to external and internal vibrations modes of $\text{Si}(\text{Al})\text{O}_4$ tetrahedrons [38,39]. The Raman spectra (Fig. 1b) exhibited a band at 1320 cm^{-1} , which is assigned to the two-phonon scattering mechanism of Fe_2O_3 [40]. The bands at 218 cm^{-1} and 285 cm^{-1} represent the internal and external phonons vibration modes of Fe_2O_3 [41]. This indicated that the Fe_3O_4 particles were oxidized to Fe_2O_3 phase in the calcination under oxidative atmosphere. XRD patterns (Fig. 1c) showed characteristic peaks of HZSM-5 at 2θ equal 7.9, 8.8, 23.0, and 24.1 and Fe_2O_3 phases at 2θ equal 24.1, 33.0, 35.5, 40.8, 49.3, 53.9, 57.5, 62.3, and 64.0. These results support the Raman results in the formation of Fe_2O_3 during calcination. The crystallite sizes of metal phase were calculated with Scherrer's equation (see Supplementary material) and the values ranged from 21 to 25 nm in the samples. The results also indicated that the calcination of the pure zeolite led to a slight increase in the crystallinity degree (5 %) but did not change the diffraction pattern. The textural properties of the uncalcined and calcined HZSM-5 and of the Fe-Z91DI catalyst were obtained from N_2 physisorption and the results are presented in Fig. 1d, Fig. S3 and Table S3. The catalyst exhibited type II isotherm with hysteresis of type IV, typical of agglomerated iron particles over the zeolites with micropores and slit-shaped mesopores. Table S3 indicates that calcination of HZSM-5 increased its surface area while maintained its pore size distribution ($d_{\text{pore}} \sim 3.6$ nm) (Fig. S3). However, impregnation with Fe resulted in a significant reduction in surface area and a change in pore diameter ($d_{\text{pore}} \sim 23.9$ nm). TEM images (Fig. 2) showed that Fe oxide particles presented an approximate size of 22.9 nm, suggesting that these particles may obstruct the zeolite pores (3.6 nm) and account for the observed decrease in surface area. [39,42].

TEM images (Fig. 2) and EDS analysis (Fig. S4) of the Fe-Z91DI catalyst indicated that the iron NPs are heterogeneously distributed on the zeolite support with regions where NPs agglomerates were detected. The catalyst displayed a particle size distribution of 5–45 nm but average particle sizes of 22.9 nm, in agreement with previously reported

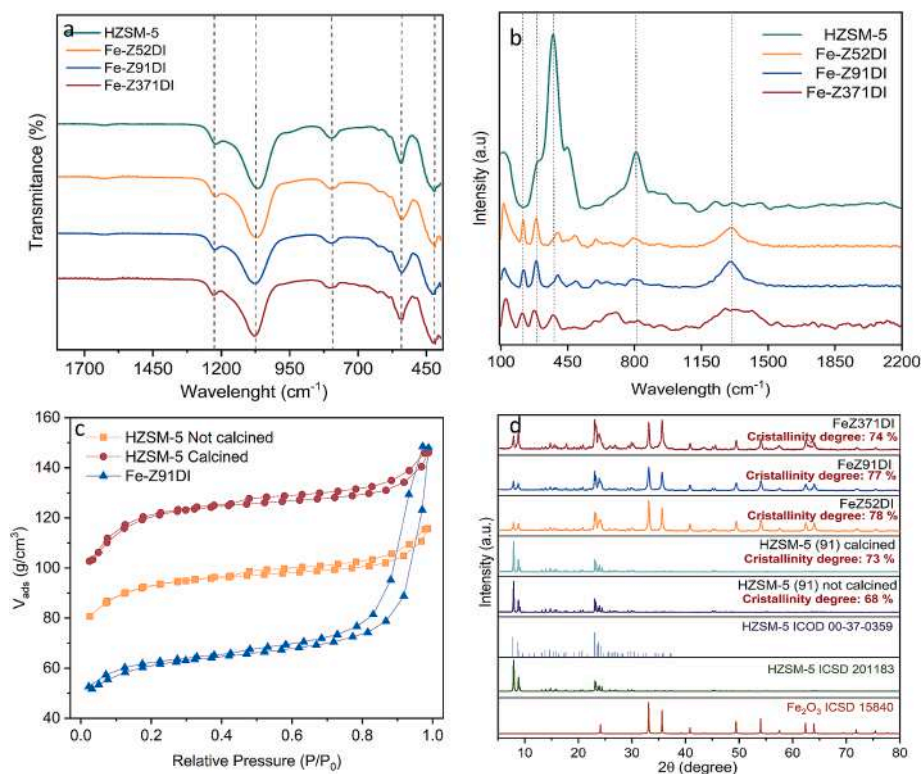


Fig. 1. (a) FTIR using attenuated total reflectance (ATR) and (b) RAMAN spectra for HZSM-5 (pure zeolite) and Fe-Z52DI, Fe-Z91DI, and Fe-Z371DI samples. (c) N_2 adsorption isotherms of Fe-Z91DI catalyst and HZSM-5 (d) XRD diffractogram of the Fe-Z52DI, Fe-Z91DI and Fe-Z371DI catalysts.

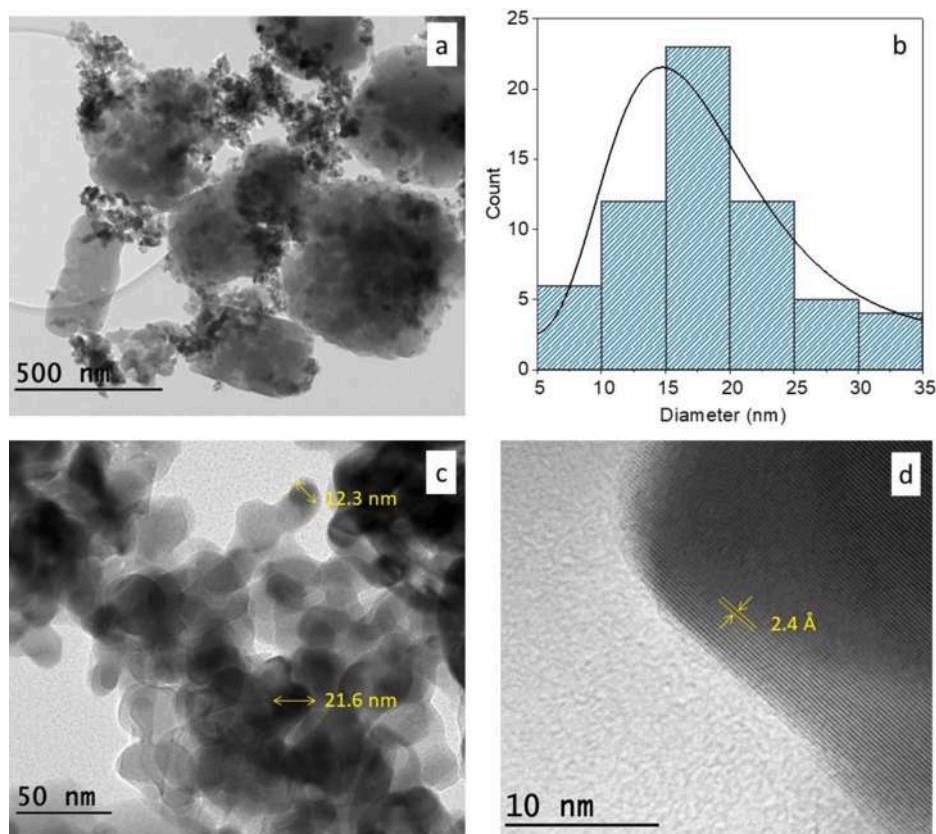


Fig. 2. TEM images of the Fe-Z91DI catalyst. (a) Full image at 500 nm. (b) Particle distribution histogram generated from 65 particle observations. (c) Zoom in image at 50 nm. (d) HRTEM image showing crystalline planes.

systems [43,44]. Elemental analysis of Fe content performed with MP AES showed 30 wt-% Fe loading for the sample Fe-Z91DI.

3.1.2. Temperature programmed reduction and chemisorption

The reduction profile of the iron oxide particles in the catalysts were evaluated from the H_2 -TPR analysis (Fig. 3a and Fig. S5). The results showed two distinct reduction peaks of iron oxide particles with increasing temperature. The first peak between 386 and 418 °C indicates the reduction of hematite to magnetite, $3Fe_2O_3 + H_2 \rightarrow 2Fe_3O_4 + H_2O$. The slight shift of the peaks for the different zeolite supports can be attributed to the different particle sizes and the metallic nanoparticles-support interactions [45]. The following broad reduction peak (450 °C and 750 °C) refers to the reduction of the magnetite: $Fe_3O_4 + H_2 \rightarrow 3FeO + H_2O$, and $FeO + H_2 \rightarrow Fe + H_2O$ [46,47]. Additionally, the FeO metastability below 600 °C is assigned to the reduction of Fe_3O_4 species into metallic Fe^0 . Hence, the multiple peaks observed in the deconvoluted curves during the final reduction stage can be explained by the presence of FeO, Fe_3O_4 , and FeO (Fig. S5) [47]. Temperature Programmed Desorption (TPD) analyses of CO_2 and NH_3 were carried out on both pure HZSM-5 (with different SiO_2/Al_2O_3) and iron catalysts for determining the basic and acid sites, respectively (Fig. 3b and c and Table S4). The HZSM-5 Z52 presented mainly weak basic sites, while the HZSM-5 Z91 and Z371 showed weak, moderate, and strong basic sites. The presence of Fe NPs on the zeolites reduced the overall amount of adsorbed CO_2 and modified the strength of zeolite basic sites. The catalysts presented a broad peak at temperatures from 170 to 230 °C, which indicates weak adsorption sites. Similar trends were observed for the acid sites on NH_3 -TPD (Fig. 3c), where iron catalysts diminished both the amount and strength of zeolite acid sites. This phenomenon is attributed to the partial masking of metal particles on the zeolite structure, which affects the accessibility of probing molecules, consistent with observations reported for metal-impregnated zeolites [48,49].

Additionally, the HZSM-5 (Z91) and Fe-Z91DI exhibited enhanced interaction with NH_3 compared to their counterparts with different SiO_2/Al_2O_3 ratios, suggesting a higher amount of accessible acid sites. Finally, CO-TPD (Fig. 3d) analysis allows evaluating CO interaction with the catalyst surface. Fig. 3d showed mostly weak and moderate interaction of CO molecule with the surface sites, and thus, capability to bind the CO adsorption on the metallic sites over a broad temperature range. The CO adsorption is influenced by both the metallic and acid-basic sites of the support [50]. The influence of the support surface was noted in Fig. 3d, which showed CO amounts decreasing with increasing zeolite SiO_2/Al_2O_3 (52 > 91 > 371). However, the strength of CO adsorption did not follow the same order. As shown, the Fe-Z91DI catalyst was different for CO adsorption, showing weaker adsorption sites in comparison to its counterparts. The Fe-Z91DI catalyst exhibited a final CO desorption peak between 315 and 560 °C, while for the Fe-Z371DI catalyst, desorption occurred between 245 and 750 °C.

3.2. Fischer-Tropsch catalytic evaluation

3.2.1. Activity tests of the Fe-Z91DI catalyst

Initially, the Fe-Z91DI catalyst was carried out for standard Fischer-Tropsch synthesis conditions, determining the CO conversion (X_{CO}) by varying the temperature. The results displayed in Fig. 4a showed that increasing the temperature results in increased activity, from 17 % at 250 °C to 86 % at 350 °C. High temperatures promote CO dissociation and Fe carbidization, which enhances the availability of C atoms on the active surface sites [51,52]. However, the CO conversion decreased returning the test to 300 °C, after reaching 350 °C, which suggests deactivation of the Fe-based catalysts, due to coke deposition, carbide oxidation, or dealumination of the zeolites [53,54]. This is in accordance with the results reported in the literature for Fe-based catalysts in FTS at higher temperatures, resulting in coke deposition [55–57]. The WGS

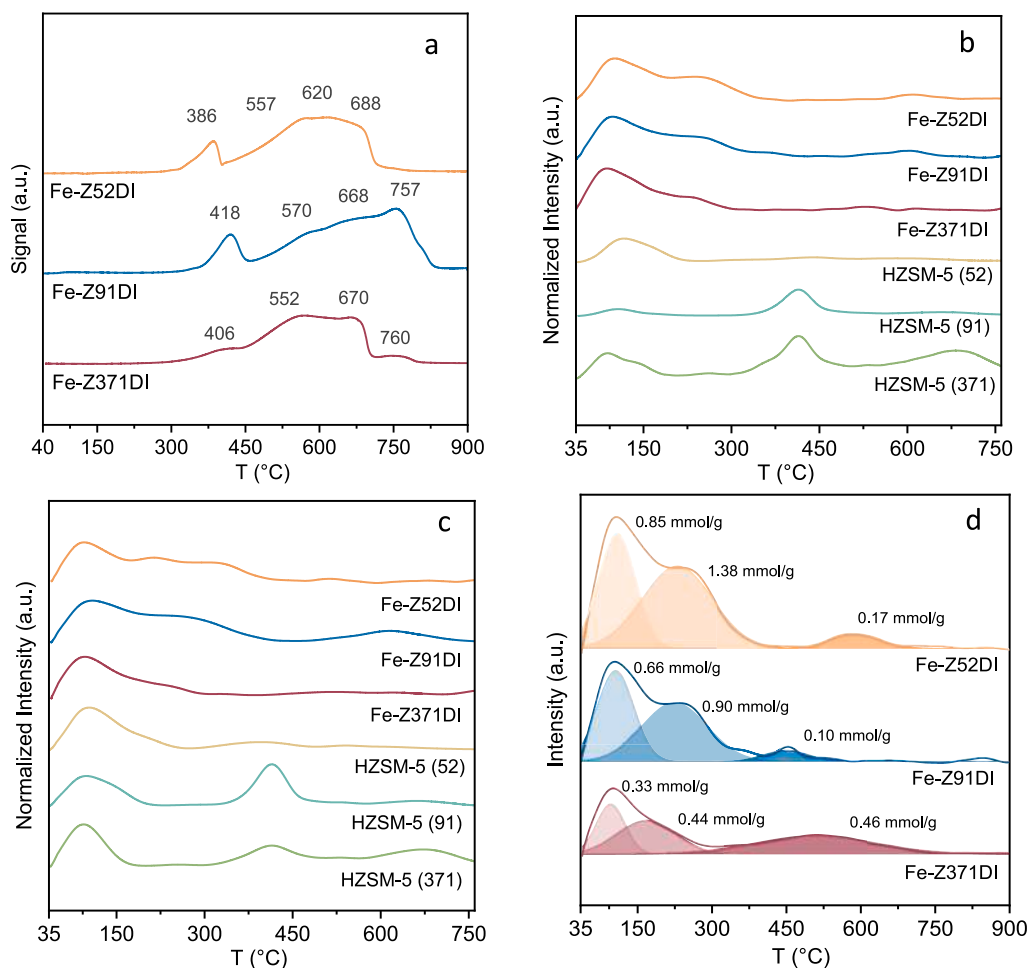


Fig. 3. Chemisorption analysis results. (a) H_2 -TPR curves. (b) CO_2 -TPD curves. (c) NH_3 -TPD curves. (d) CO -TPD curves.

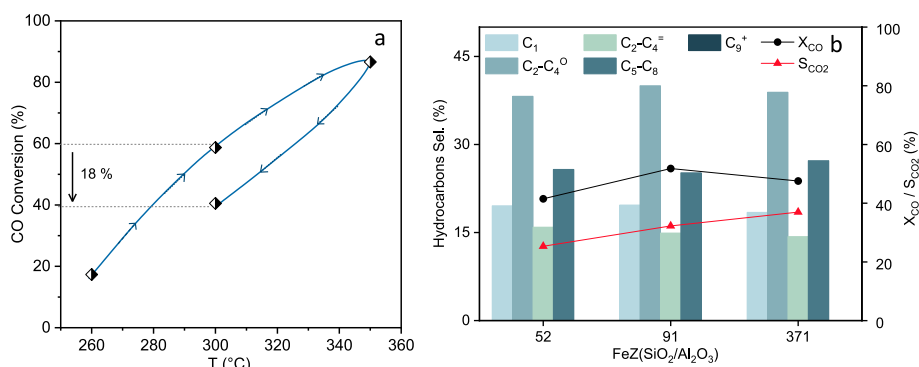


Fig. 4. (a) Conversion of CO of the Fe-Z91DI catalyst at 20 bar, $H_2/CO = 2$ and $WHSV = 6880 \text{ mL} \cdot \text{g}^{-1} \cdot \text{h}^{-1}$. (b) Effect of HZSM-5 SiO_2/Al_2O_3 ratio on FTS activity and product distribution, excluding CO_2 . Fe-Z52DI, Fe-Z91DI and Fe-Z371DI catalysts at 300 °C, 20 bar, $H_2/CO = 2$ and $WHSV = 6880 \text{ mL} \cdot \text{g}^{-1} \cdot \text{h}^{-1}$.

reaction is favored at higher temperatures, since the selectivity to CO_2 (S_{CO_2}) increased, as shown in Fig. S7. The pure zeolite was also tested under the same conditions but did not exhibit significant catalytic activity, as shown in Fig. S9.

3.2.2. Influence of the zeolites SiO_2/Al_2O_3 ratio on the FTS

The influence of the SiO_2/Al_2O_3 ratio of HZSM-5 on CO conversion and product distribution was investigated at 300 °C. The results in Fig. 4b and Fig. S8 showed that SiO_2/Al_2O_3 ratios of the catalysts influenced the conversion of CO (X_{CO}) and the selectivity to CO_2 (S_{CO_2}) at 300 °C, and they were relatively stable with TOS of 6 h (Fig. S8).

However, the Fe-Z52DI exhibited lower X_{CO} conversion than Fe-Z91DI and Fe-Z371DI, while the CO_2 selectivity followed the order: Fe-Z371DI > Fe-Z91DI > Fe-Z52DI. Note that the SiO_2/Al_2O_3 ratio did not influence the selectivity to hydrocarbons (HCs), as shown in Fig. 4b. The selectivity of the C_2 - C_4 , excluding CO_2 , is approximately 55 %, and similar for different zeolite SiO_2/Al_2O_3 ratios. The selectivity of C_1 is of the order of 20 %, while the selectivity of C_9^+ , about 25 %. The higher X_{CO} of Fe-Z91DI catalyst suggests that the SiO_2/Al_2O_3 of Z91 influenced CO conversion and was the best ratio for enhancing the light HC production, which can be attributed to the acidity (Fig. 3b and Fig. 3c and Table S4) with predominantly strong acid sites compared to the weak

and moderate acid sites. From Table S4, both the pure zeolite and the $\text{SiO}_2/\text{Al}_2\text{O}_3$:91 impregnated catalyst exhibited a considerable higher amount of adsorbed NH_3 , indicating a greater number of acidic sites in this material. Thus, it is believed that the higher number of acidic sites on the surface of this material may have favored CO conversion. Liu et al. [50] reported the influence of balanced strong, medium, and weak acid sites for catalysts to improve the oligomerization and cracking reactions and to prevent coke deposition. However, Fe-Z91DI displayed the highest influence of the strong acid sites but lower weak and medium acid sites, in opposition to the other Si/Al ratios, according to the NH_3 -TPD analysis. Moreover, CO-TPD results showed that Fe-Z91DI presented weak adsorption sites for CO, compared to the Fe-Z52DI and Fe-Z371DI catalysts, which supports that the balanced CO adsorption strength favored its activity. Regarding CO_2 selectivity from WGS, a trend can also be observed with the number of basic sites in the CO_2 TPD analysis. The Z371 sample exhibited the lowest amount of adsorbed CO_2 , indicating a lower presence of basic sites resulting in lower CO_2 selectivity in the catalytic tests [30]. Therefore, the Fe-Z91DI catalyst was studied for further investigating reaction conditions, stability, and kinetic modeling. The TOF (turnover frequency) value of Fe-Z91 DI was calculated and was of approximately $4.78 \times 10^{-1} \text{ s}^{-1}$.

Overall, the variations in activity and CO_2 selectivity with different $\text{SiO}_2/\text{Al}_2\text{O}_3$ ratios underline the complex interplay between the zeolite's acidity and the catalytic processes. The acidity can also affect the surface reactions and intermediate species' stability. A higher acidity might favor pathways that lead to CO_2 formation from WGS, thus explaining the higher CO_2 selectivity with lower $\text{SiO}_2/\text{Al}_2\text{O}_3$ ratios. The minor impact of $\text{SiO}_2/\text{Al}_2\text{O}_3$ ratios on hydrocarbon selectivity suggests that the primary hydrocarbon formation pathways are not significantly altered by the changes in acidity within the studied range. This indicates that the bifunctional nature of the catalyst is robust across different acidity levels.

3.2.3. Investigation of reaction conditions

For the Fe-Z91DI catalyst, the influence of the operating conditions, such as temperature, pressure, feed composition, and space velocity,

were investigated, as presented in Fig. 5.

Overall, the hydrocarbon distribution for this catalyst showed a major production of short chain hydrocarbons (C_2 - C_4), 47–61 %, followed by medium chain hydrocarbons within the gasoline range (C_5 - C_8), 0–37 %, methane (C_1), 0–37 %, and long chain hydrocarbons (C_9 - C_{12}), 0–5 %. Fig. 5a allows observing that temperature influenced the conversion of CO, selectivity of CO_2 and the hydrocarbons distribution. The catalyst evaluated at 260 °C presented X_{CO} and S_{CO_2} values of 13 % and 12 %, respectively, but increased significantly for 320 °C, reaching 66 % and 35 %, respectively. This can be attributed to increasing CO dissociation on the metallic active sites. The WGS occurs above 300 °C due to the Fe_3O_4 active phase [37]. The hydrocarbons distribution was influenced by increasing temperature, favoring the formation of short hydrocarbon chains. This is because high temperatures favor the HC chain termination step, which has higher activation energy compared to the propagation step, decreasing the α -value [58,59], as observed in the fitted ASF curves (Fig. S10). Moreover, the *in-situ* formation of various iron carbide species at different temperatures plays a crucial role in hydrocarbon chain growth. There is still debate in the literature regarding the influence of different carbides (such as χ - Fe_5C_2 , θ - Fe_3C , Fe_7C_3 , ε - Fe_2C , and ε' - Fe_2C_7) on FTS results, but it is generally accepted that they can change product selectivity [60]. The space velocity directly influences the contact time. Fig. 5b shows that the CO conversion increased from 40 % to 58 %, changing the WSHV from 9000 to 4000 $\text{mL.g}^{-1}.\text{h}^{-1}$, while the production of liquid hydrocarbons augmented from 26 % to 37 %, respectively, and the selectivity of methane and light HCs (C_2 - C_4) decreased. As reported in the literature, the decrease of space velocity influences the product distribution by favoring the chain growth [61]. Regarding the pressure effect on activity, the literature reports that increased pressure favors the conversion of CO [51,61,62], in agreement with the results displayed in Fig. 5c. The CO conversion increased from 10 % at 1 bar to 63 % at 30 bar. Also note the increasing conversion of CO from 1 and 10 bar. The pressure effect on the hydrocarbon distribution is still under debate in the literature, but it is generally accepted that by increasing the pressure, the methane formation diminishes [63]. Fig. 5c shows that the selectivity of

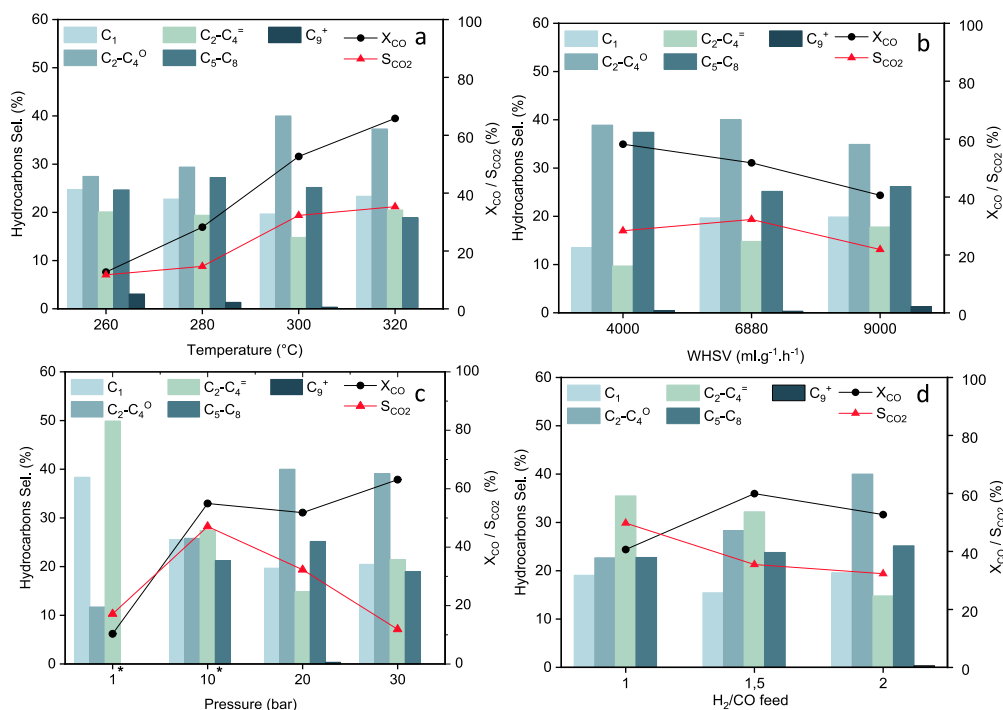
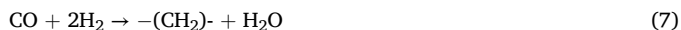


Fig. 5. Effect of reaction conditions on FTS activity and product distribution with Fe-Z91DI catalyst. (a) Temperature effect at 20 bar, $\text{H}_2/\text{CO} = 2$ and $\text{WHSV} = 6880 \text{ mL.g}^{-1}.\text{h}^{-1}$. (b) Space velocity effect at 300 °C, 20 bar and $\text{H}_2/\text{CO} = 2$. (c) Pressure effect at 300 °C, $\text{H}_2/\text{CO} = 2$ and $\text{WHSV} = 6880 \text{ mL.g}^{-1}.\text{h}^{-1}$ and $^*4000 \text{ mL.g}^{-1}.\text{h}^{-1}$. (d) Feed composition effect at 300 °C, 20 bar and $\text{WHSV} = 4000 \text{ mL.g}^{-1}.\text{h}^{-1}$.

CH₄ (S_{CH₄}) decreased from 38 % to 25 % with increasing pressure of 1 bar to 10 bar. De la Peña O'Shea et al. [64] observed that $-CH_x$ increased (Eq. (7)) with pressure and favored the production of higher hydrocarbon chains.



However, this behavior was not observed here, as shown in Fig. 5c, which did not change the selectivity of HC with increasing pressure between 20 and 30 bar. Botes et al. [65] reported that pressure variation presented low influence on product selectivity for Fe-based catalysts, in accordance with our results. Note that the syngas composition significantly affected the CO conversion and CO₂ selectivity. Fig. 5d showed an increasing CO conversion from 41 % to 59 % by increasing hydrogen in the feed composition. FTS often exhibits low X_{CO} in poor hydrogen environments, as the P_{H₂} significantly influences the kinetics of Fe-based catalysts, as reported in the literature [66]. The WGS reaction decreased as the selectivity of CO₂ decreased from 49 % to 32 % by increasing the H₂/CO feed ratio. This was attributed to the equilibrium nature of the WGS (Eq. (4)), which shifts the reaction toward CO production instead of CO₂. A similar result was reported by Burgun et al. [67] on Fe-Cu/Y-zeolite catalysts for FTS.

3.2.4. Stability test and post-reaction characterization

The stability test of the Fe-Z91DI catalyst was performed with time on stream for 72 h and the results are shown in Fig. 6. They showed excellent stability under evaluated conditions (X_{CO} ~ 63) and low deactivation for longer times. The deactivation occurred at the beginning, when the X_{CO} decreased from 68 % to 55 %, remaining stable until the end. This can be attributed to the coke deposition on very active metallic sites, as reported previously [67]. Additionally, there was a slight increase in X_{CO} above approximately 40 h testing onwards, which may be due to the influence of time on the formation of active Fe₅C₂ phases [68].

RAMAN and XRD analyses of the fresh and spent catalyst are displayed in Fig. S12a and b respectively. The Raman spectra did not show any carbon-carbon vibration bands, indicating insignificant coke deposition. The XRD data in Fig. S12b showed the presence of HZSM-5 peaks in the spent catalyst, indicating that the main structure of the zeolite was preserved after the reaction. However, it is noteworthy that the crystalline iron oxide phases were no longer present in the post-reaction catalyst, and slight peaks appeared between 2θ 41° and 47°, indicating iron carbide phases. According to Weckhuysen et al. [69], the XRD pattern of iron carbide particles after reaction presents a challenging issue due to the small particle sizes formed. Indeed, the low intensity and broadened peaks observed in the carbides region aligns

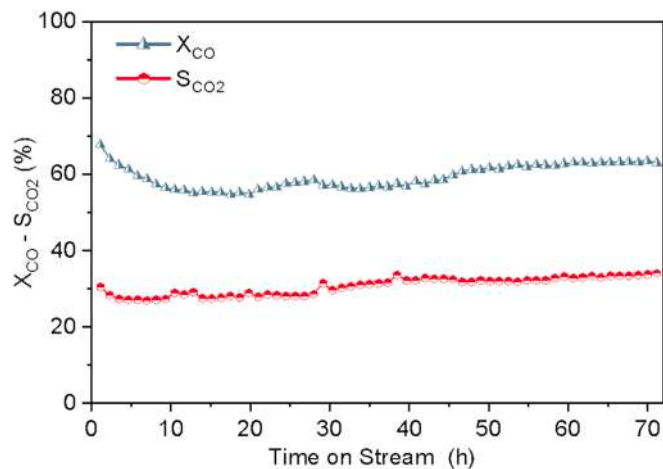


Fig. 6. Time on stream test for FTS with Fe-Z91DI catalyst. T: 300 °C, P: 20 bar, H₂/CO = 2, WHSV = 4000 mL.g⁻¹.h⁻¹.

with this observation. Thus, to accurately evaluate Fe species on the catalyst surface, a Mossbauer spectroscopy was conducted on the spent catalysts, and the results are presented on Fig. 7 and Table S6.

As shown in Fig. 7, post-reaction catalyst presented the coexistence of different Fe sites, such as Fe₃O₄, Fe₅C₂ and Fe₃C. This observation confirms the formation of Fe carbides on the catalyst surface during the FT reaction. Typically, Fe oxide carburization occurs when CO interacts with the catalyst, forming carbide species, whose stability depends on the FTS environment, including temperature and the presence of H₂O and CO₂[70]. The data in Table S6 indicates the formation of 56.4 % of Fe₅C₂, which is the most active phase for FT reaction. Additionally, recent studies have shown that the Fe₅C₂ phase exhibits lower hydrogenation capacity and higher activity for the chain growth step during FTS [71,72]. In addition to Fe₅C₂, Fe₃C was found to constitute 11.7 % of the spent catalyst. The role of Fe₃C in FTS is still controversial, with some authors associating it with catalyst deactivation, while others consider it active for CO conversion [73].

The TEM image of the post-reaction catalyst (Fig. 8) showed an increase in the average particle diameter from 22 nm in the fresh catalyst to 29 nm. Additionally, no filaments of amorphous coke were observed. TGA analysis of the post-reaction catalyst was also conducted, and the results are presented in Fig. S13. The catalyst exhibited a low mass loss of 3.8 %, with a slight increase in mass up to 1.0 % during the analysis, which aligns with the exothermic DTA events, suggesting carbon decomposition.

3.3. Fischer-Tropsch kinetic assessment

To ensure the quality of the collected kinetic data, the effects of mass transfer in the catalytic bed were initially studied using the X_{CO} vs W/F curve and the calculated Mear's external mass transfer and Weisz-Prater's internal mass transfer criteria. The results are presented in Fig. 9 and Table S1.

Fig. 9 presents the CO conversion as a function of W/F, for experiments using different catalyst masses. The higher X_{CO} and its short variation at higher W/F values indicate the dominance of the diffusional regime. Conversely, lower X_{CO} value at lower W/F indicates the proximity to establishing the kinetic regime. Then, based on Weisz-Prater and Mears criteria (Table S1), and on the results from Fig. 9, the reactional system was set to operate at a WHSV of 160000 mL.g⁻¹.h⁻¹ within the kinetic regime. Table S7 presents the collected kinetic data and the results of CO conversion used for model fitting. The experimental results from Table S7 showed X_{CO} values ranging from 4.76 % to 19.77 % with

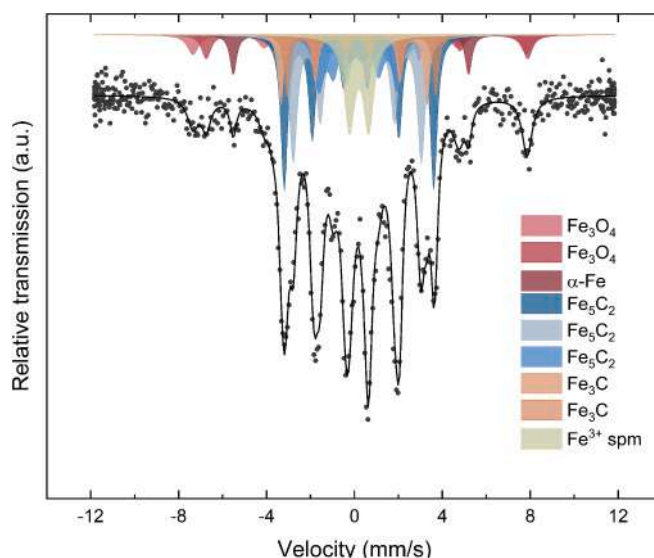


Fig. 7. Post-reaction Mössbauer spectroscopy of the Fe-Z91DI catalyst.

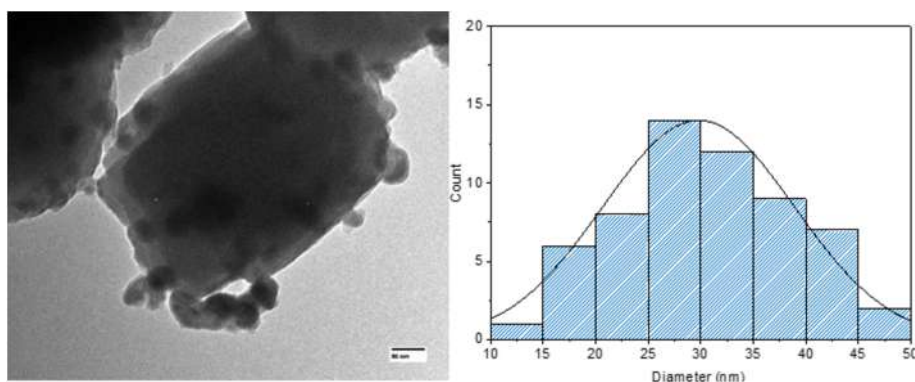


Fig. 8. Post-reaction TEM of the Fe-Z91DI catalyst. a) TEM image at 500 nm. b) Particle distribution histogram generated from 61 particle observations.

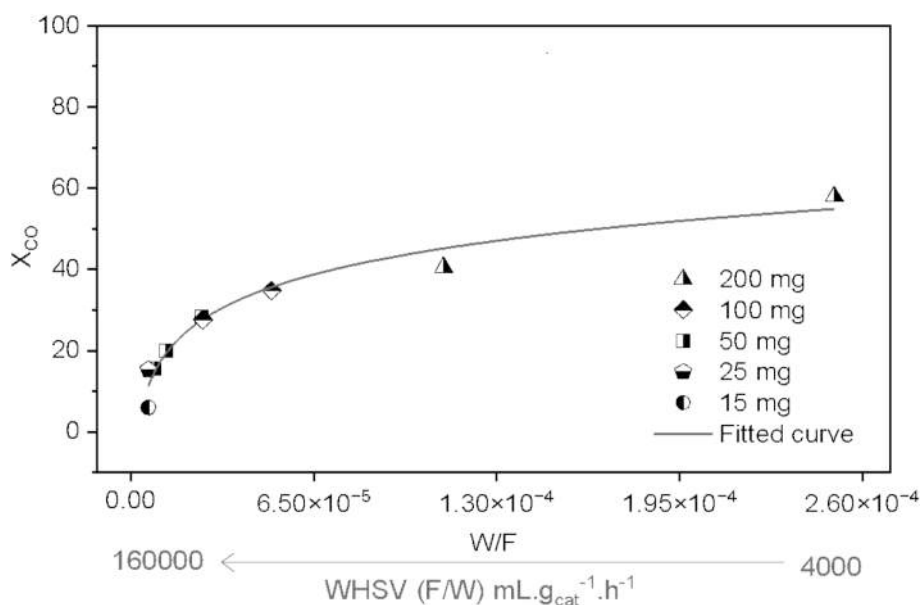
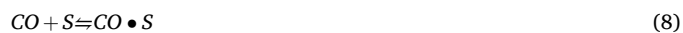


Fig. 9. W/F vs X_{CO} curve of the Fe-Z91DI catalyst at 300 °C, 20 bar, H_2/CO : 2, WHSV: 4000, 9000, 20000, 40000, 80000, 120,000 and 160000 $mL.g^{-1}.h^{-1}$.

both temperature and components partial pressure affecting the CO consumption rate. As known, FTS mechanisms can follow several routes by distinguishing the monomer structure responsible for chain growth initiation [36]. Thus, 10 different LHHW models for FTS with Fe-based catalysts considering the influence of CO, H_2 , CO_2 , or H_2O on the adsorption term, associative or dissociative adsorption mechanisms and the reaction sites (single or double) were selected from literature to fit the experimental data (Table S7). Table 2 shows the results of the non-linear regression.

It is important to highlight that there is limited research on kinetic modeling for FTS using Fe/zeolite catalysts. The models in Table 2 were thus primarily designed for simple Fe-based catalysts, with the exception of model 8, which is for Fe over zeolite catalysts. Overall, the models studied exhibited a correlation parameter R^2 ranging from 0.67 to 0.92, and the estimated parameters were found to be physically plausible. To facilitate the discussion, the models can be classified into groups: 1 – those incorporating H_2O adsorption on the surface (models 4, 5, 9, and 10), 2 – those involving CO_2 adsorption on the surface (models 1, 2, and 3), and 3 – those neglecting CO_2 adsorption (models 6, 7, and 8). Models from group 1 presented the worst fit, particularly the models 4, 5, and 10, however the model 9 showed a reasonable fit. The pre-exponential adsorption constant of approximately 10^{-36} suggests that water minimally impacts this catalyst reaction rate. It indicates rapid desorption or consumption of formed water on the catalyst surface. Indeed, water

adsorption is still a topic of debate in the literature in FTS kinetic studies. The first kinetic models developed for FTS (for example, model 4), accounts for water adsorption on the inhibition term [78]. Nevertheless, kinetic studies carried out by Sasol revealed that the apparent water inhibition strongly depends on the feed gas composition [81]. Similarly to our findings, Nikbakht, Mirzaei, and Atashi [35] studied a Fe-Co-Ce/Zeolite catalyst and reported that CO consumption rate was better described by models disregarding water adsorption. The authors also reported that CO exhibited three times greater adsorption than H_2O on the catalyst surface. Models from group 2 presented the best fit compared to models from group 3. Ledakowicz et al. [76] presented similar results, which suggests a competitive chemisorption of CO and CO_2 (formed from WGS) takes place on the active sites, as described by Eqs. (8) and (9).

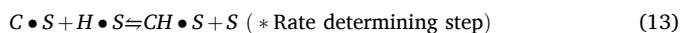


Among the models from group 2, the model 3 differs from models 1 and 2 by considering a single site mechanism and an associative adsorption of CO molecules; however, this model presented the worst fit compared to the other two. Consequently, based on the statistical parameters, the model 1 [74] exhibited the best fit for the Fe-Z91DI catalyst and was chosen as the model of CO consumption for this

Table 2
Results of fitted kinetic models for CO conversion on Fe-Z91DI catalyst.

Model	k_0	E_a (kJ/mol)	k_{10}	$H_{ads(1)}$ (kJ/mol)	k_{20}	$H_{ads(2)}$ (kJ/mol)	Statistical parameters R^2 F RMSE			Ref
1 $r = \frac{kpH_2^{0.5}pCO^{0.5}}{(1 + K_1pCO^{0.5} + K_2pCO_2)^2}$	$1.16 \cdot 10^6$	78.583	$5.56 \cdot 10^2$	-17.778	$7.00 \cdot 10^{-8}$	-98.8112	0.923	84.78	0.00057	[74]
2 $r = \frac{kpH_2^{0.5}pCO}{(1 + K_1pCO^{0.5} + K_2pCO_2)^2}$	$9.45 \cdot 10^6$	69.903	$2.42 \cdot 10^0$	-13.678	$3.29 \cdot 10^{-8}$	-112.540	0.911	73.56	0.00061	[75]
3 $r = \frac{kpH_2pCO}{(pCO + K_2pCO_2)}$	$3.31 \cdot 10^4$	83.697	–	–	$1.68 \cdot 10^{-4}$	-60.403	0.830	61.91	0.00081	[76]
4 $r = \frac{kpH_2pCO}{(pCO + K_2pH_2O)}$	$5.31 \cdot 10^4$	87.588	–	–	$8.99 \cdot 10^{-2}$	-8.997	0.727	33.76	0.00103	[77]
5 $r = \frac{kpH_2^2pCO}{(K_1pCOpH_2 + pH_2O)}$	$1.00 \cdot 10^5$	52.340	$1.27 \cdot 10^0$	-37.474	–	–	0.723	33.10	0.00104	[78]
6 $r = \frac{kpH_2pCO^{0.5}}{(1 + K_1pCO)^2}$	$4.90 \cdot 10^5$	76.731	$2.23 \cdot 10^3$	-16.694	–	–	0.858	76.92	0.00740	[66]
7 $r = \frac{kpH_2pCO}{(1 + K_1pCO)^2}$	$4.90 \cdot 10^3$	76.476	$2.24 \cdot 10^3$	-16.694	–	–	0.832	62.91	0.00081	[79]
8 $r = \frac{kpH_2pCO}{(1 + K_1pCO + K_2pH_2)^2}$	$5.12 \cdot 10^5$	81.342	$4.97 \cdot 10^0$	-35.554	$6.31 \cdot 10^2$	-11.222	0.870	48.33	0.00073	[35]
9 $r = \frac{kpH_2pCO}{(1 + K_1pCO + K_2pCO_2 + K_3pH_2O)}$	$3.01 \cdot 10^7$	70.192	$8.27 \cdot 10^0$	-34.318	$k_2: 6.31 \cdot 10^{-6}$ $k_3: 8.06 \cdot 10^{-36}$	$H_{ads(2)}: -128.048$ $H_{ads(3)}: -46.307$	0.910	47.15	0.00064	[80]
10 $r = \frac{kpH_2^{0.5}pCO}{(1 + K_1pCO + K_2pCO_2 + K_3pH_2O)^2}$	$1.49 \cdot 10^3$	55.000	$2.34 \cdot 10^1$	-5.789	$k_2: 5.86 \cdot 10^{-5}$ $k_3: 2.54 \cdot 10^{-9}$	$H_{ads(2)}: -61.399$ $H_{ads(3)}: -37.793$	0.670	9.86	0.00120	[80]

catalyst. This kinetic model is based on the carbide mechanism and sets for a dissociative adsorption of CO and H₂ molecules, however, the CO adsorption on Fe active sites is stronger when compared to H₂. It also considers the irreversible formation of the monomer intermediate (-CH-) as the rate-determining step (RDS), a competitive adsorption of CO₂ and CO, and a double site mechanism, as shown in Eqs. (10)–(15).



In the mathematical development from the reactions step, Eq. (16) is obtained, where k' represents a kinetic constant, and K a equilibrium constant [74]:

$$r_{CO} = \frac{k'pH_2^{0.5}pCO^{0.5}}{(1 + K_{CO}pCO^{0.5} + K_{CO_2}pCO_2)^2} \quad (16)$$

where the kinetic constants and adsorption equilibrium constants are temperature-dependent and are assumed to follow the Arrhenius law (Eq. (17)) and Van't Hoff law (Eqs. (18) and (19)), respectively:

$$k = k_0 e^{\left(\frac{-E_a}{R.T}\right)} \quad (17)$$

$$K_{CO} = k_0 e^{\left(\frac{H_{adsCO}}{R.T}\right)} \quad (18)$$

$$K_{CO_2} = k_{CO_2} e^{\left(\frac{H_{adsCO_2}}{R.T}\right)} \quad (19)$$

where E_a is the reaction activation energy, k_0 , k_{CO_0} and k_{CO_2} are the pre-

exponential factors, and H_{adsCO} , H_{adsCO_2} are the adsorption enthalpies of CO and CO₂, respectively. Overall, experimental and theoretical CO consumption rates obtained from model 1 presented a reasonable correlation (Fig. S16) and the residual analysis exhibited a normal distribution with a consistent error variability across the observations in Figs. S14 and S15.

The determined activation energy for model 1 was of 78.85 kJ/mol. Eshraghi, Mirzaei, and Atashi [82] pointed out that most FTS models exhibit E_a values from 63 to 132.3 kJ/mol, due to the different mass transfer conditions encountered in the studies. Additionally, the calculated enthalpies for CO and CO₂ adsorption were -17.78 kJ/mol and -98.81 kJ/mol, respectively, confirming the expected exothermic nature of the adsorption phenomena [82]. Fig. 10 presents the fitting results and behavior of model 1 at different temperatures and compositions. The results showed the increasing CO consumption rate with increasing temperature, as expected, since reaction kinetic constant is considered to follow Arrhenius's law. Hydrogen partial pressure was also determinant on for the CO consumption rate. Dry, Shingles, and Boshoff [83] proposed that for CO conversions below 60 %, the FTS reaction rate was primarily affected by pH₂, which can be expressed by a power law according to Eq. (20). An increase in the reaction rate is correlated with high H₂ concentration in the feed, as evidenced in Table S5. However, in this work the power law model was fitted to the experimental data, but it showed R^2 and RMSE values of 0.7 of 0.001, respectively. Therefore, the LHHW models, which integrate the adsorption of various species on the catalyst surface, presented a better fit to the data.

$$-r'_{co} = kpH_2^a \quad (36)$$

3.3.1. Drifts-in situ analysis

Diffuse Reflectance Infrared Fourier Transform Spectroscopy in-situ (DRIFTS-in situ) analysis under FTS conditions was conducted for Fe-Z91DI to support the reaction mechanism proposed for the model 1. Fig. 11 displays the spectra for different temperatures and pressure of 8 bar. The adsorption bands in the range between 1800 and 2100 cm⁻¹ are attributed to CO adsorbed molecules. Typically, CO molecules adsorb on various sites on the catalyst surface, presenting either linear adsorption (associative CO adsorption mechanism) or bridging adsorption across

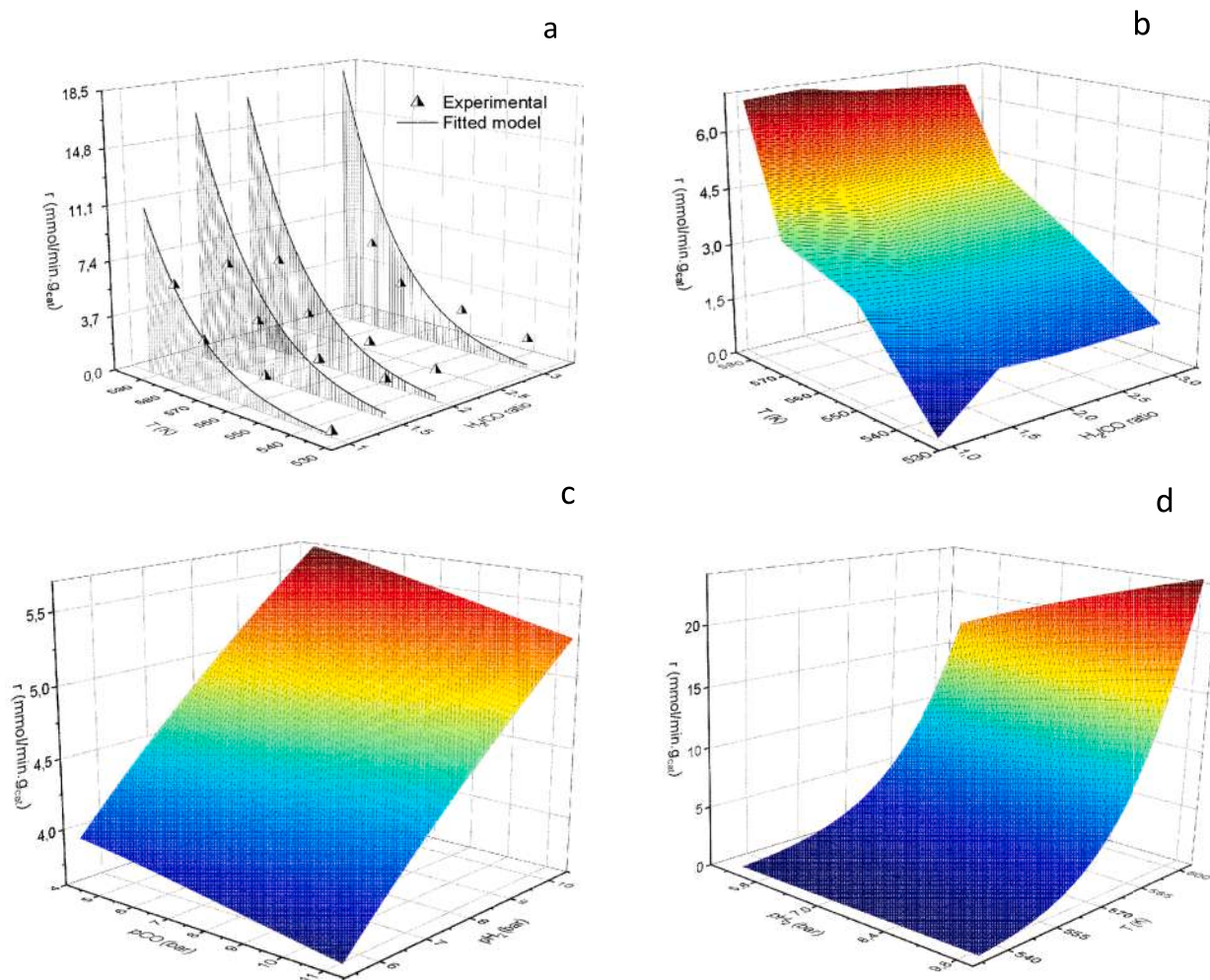


Fig. 10. Model 1 adjustment and behavior of CO consumption rate. (a) Experimental data and model 1 predicted curves. (b) Surface response of model 1 evaluating temperature and H₂/CO ratio. (c) influence of P_{CO} and P_{H₂} on CO consumption rate. (d) Influence of temperature and P_{H₂} on CO consumption rate.

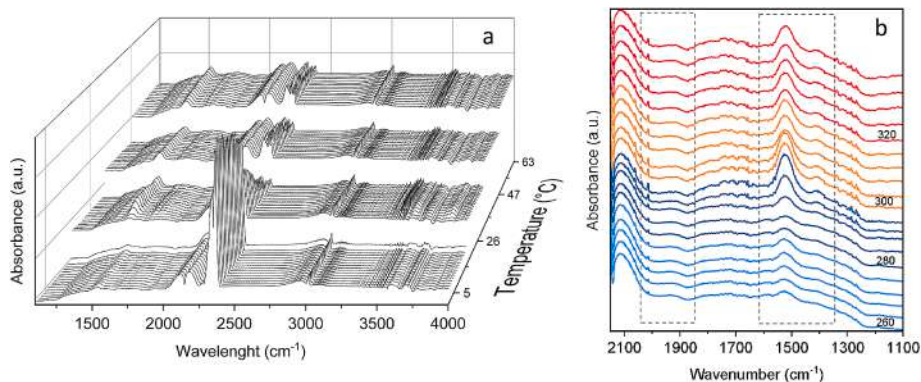


Fig. 11. DRIFTS-in situ FTS analysis of Fe-Z91DI catalyst at 8 bar, H₂/CO: 2 and WHSV: 4000 mL.g⁻¹.h⁻¹. a) 1100 – 4000 cm⁻¹ 3D plot. b) 1100 – 2150 cm⁻¹ CO and CO₂ adsorbed region.

two adjacent sites (dissociative CO adsorption mechanism) [80]. The slightly broad band in the range 1877–1965 cm⁻¹ is assigned to CO adsorbed in the bridge configuration, whereas the small band at 2012 cm⁻¹ corresponds to CO linearly-adsorbed species [82,84]. Thus, the occurrence of CO-bridged molecules supports the dissociative adsorption path of CO proposed in Eqs. (11)–(12) of the proposed model. Additionally, when CO₂ adsorbs on a metal surface, its intermediates adsorption may include chelating or bridging bidentate carbonates,

monodentate carbonates, or linearly coordinated CO₂ molecules, which are found in 1707 to 1366 cm⁻¹ range [85]. Particularly, the bands observed at 1524 cm⁻¹ and 1415 cm⁻¹ are indicative of bidentate and monodentate carbonate species, respectively [86,87], which suggests CO₂ adsorption on active sites, as set by the model in Eq. (32). Furthermore, as expected, these bands were more intense for temperatures above 260 °C, since the studied catalyst presented increased selectivity for CO₂ at higher temperatures. Finally, the adsorption bands

in a region between 2700 to 3200 cm^{-1} are ascribed to C-H bonding hydrocarbons, and bands in the range 2848–3166 cm^{-1} are typical of bands of gaseous CH_4 molecules [88]. A summary of the main species related to the adsorption results from Fig. 11 is presented in Table S8.

4. Conclusions

This study investigated Fe/HZSM-5 catalysts for Fischer-Tropsch synthesis by combining characterization, reaction condition optimization, and kinetic modeling. The data confirmed the presence of crystalline Fe_2O_3 and zeolite phases after calcination. The catalyst exhibited a high surface area with mesopores and an average particle size of 22.9 nm. Notably, iron impregnation modified the moderate acidity of the zeolite supports. Among various $\text{SiO}_2/\text{Al}_2\text{O}_3$ ratios, Fe-Z91DI achieved the best FTS performance, with a CO conversion exceeding 50 % and a selectivity for $\text{C}_5\text{-C}_8$ hydrocarbons (gasoline range) of up to 37 % at 300 °C. While temperature enhanced CO conversion, it also increased CO_2 selectivity. Pressure and H_2/CO molar feed ratio influenced both CO conversion and CO_2 selectivity, but not the product distribution. Importantly, the catalyst showed stable activity over a 72-hour reaction. Kinetic modeling revealed that CO consumption on Fe-Z91DI followed a Langmuir-Hinshelwood-Hougen-Watson (LHHW)-type model. The model considers dissociative adsorption of CO and H_2 , followed by their reaction on separate sites to form the rate-determining step (RDS) product, the monomer ($-\text{CH}_x-$). In-situ DRIFTS analysis supported the competitive adsorption between CO and CO_2 on the active sites. This work establishes a link between Fe/HZSM-5 physicochemical features, reaction conditions, and FTS performance. The kinetic analysis provides valuable insights into the CO activation mechanism specific to this catalyst type, aiding future optimization and catalyst design. Future research directions include exploring alternative synthesis methods to investigate particle size effects, modifying zeolite porosity for improved hydrocarbon selectivity, and optimizing catalyst composition with promoters.

CRedit authorship contribution statement

Lucas Alves da Silva: Writing – original draft, Methodology, Investigation, Formal analysis, Data curation. **Vilma Heczko:** Writing – review & editing, Investigation, Formal analysis. **Martin Schmal:** Writing – review & editing, Validation, Supervision, Methodology, Formal analysis. **Pedro Henrique Cury Camargo:** Writing – review & editing, Validation, Supervision, Project administration, Methodology, Formal analysis, Conceptualization. **Rita Maria Brito Alves:** Writing – review & editing, Validation, Supervision, Resources, Formal analysis, Conceptualization. **Reinaldo Giudici:** Writing – review & editing, Validation, Supervision, Project administration, Funding acquisition, Formal analysis, Data curation, Conceptualization.

Declaration of competing interest

The authors declare that they have no known competing financial interests or personal relationships that could have appeared to influence the work reported in this paper.

Acknowledgments

The authors gratefully acknowledge the São Paulo Research Foundation (FAPESP), Brazil, (grant numbers 2019/12856-3, 2021/05329-7, 2022/07813-6, 2022/04751-0, and 2023/01969-7) and the European Union's research and innovation funding programme Horizon 2020, Belgium, (4AirCRAFT project, grant number 101022633) for their financial support. The authors also thank the National Council for Scientific and Technological Development (CNPq), Brazil, (grant numbers 310125/2021-9, 314598/2021-9). This study was financed in part by the Coordination for the Improvement of Higher Education Personnel

(CAPES), Brazil, (Finance Code 001). P.H.C.C thanks Aron Jagielski and Pedro Muñoz Rodríguez for the support with the preparation of some catalysts. The authors are also grateful to Prof. Mariella Camarena and Prof. Dalber Candela for their technical support in the Mossbauer spectroscopy analysis.

Appendix A. Supplementary data

Supplementary data to this article can be found online at <https://doi.org/10.1016/j.cej.2025.159203>.

Data availability

Data will be made available on request.

References

- [1] IEA, World Energy Outlook, Paris, 2023, accessed January 28, 2024, <https://www.iea.org/reports/world-energy-outlook-2023>, 2023.
- [2] bp, Statistical Review of World Energy, (2022). https://www.bp.com/en/global/corporate/energy-economics/statistical-review-of-world-energy.html#tab_sr-2022 (accessed January 28, 2024).
- [3] P. Roy, A.K. Mohanty, M. Misra, Prospects of carbon capture, utilization and storage for mitigating climate change, *Environ. Sci.: Adv.* (2023), <https://doi.org/10.1039/D2VA00236A>.
- [4] W. Chen, T. Lin, Y. Dai, Y. An, F. Yu, L. Zhong, S. Li, Y. Sun, Recent advances in the investigation of nanoeffects of Fischer-Tropsch catalysts, *Catal. Today* 311 (2018) 8–22, <https://doi.org/10.1016/j.cattod.2017.09.019>.
- [5] W. Shafer, M. Gnanamani, U. Graham, J. Yang, C. Masuku, G. Jacobs, B. Davis, Fischer-Tropsch: Product Selectivity—The Fingerprint of Synthetic Fuels, *Catalysts* 9 (2019) 259, <https://doi.org/10.3390/catal9030259>.
- [6] M. Martinelli, M.K. Gnanamani, S. LeViness, G. Jacobs, W.D. Shafer, An overview of Fischer-Tropsch Synthesis: XTL processes, catalysts and reactors, *Appl. Catal. A* 608 (2020) 117740, <https://doi.org/10.1016/j.apcata.2020.117740>.
- [7] P.K. Gupta, V. Kumar, S. Maity, Renewable fuels from different carbonaceous feedstocks: a sustainable route through Fischer-Tropsch synthesis, *J. Chem. Technol. Biotechnol.* 96 (2021) 853–868, <https://doi.org/10.1002/jctb.6644>.
- [8] R. Guettel, U. Kunz, T. Turek, Reactors for Fischer-Tropsch Synthesis, *Chem. Eng. Technol.* 31 (2008) 746–754, <https://doi.org/10.1002/ceat.200800023>.
- [9] J. van de Loosdrecht, F.G. Botes, I.M. Ciobica, A. Ferreira, P. Gibson, D.J. Moodley, A.M. Saib, J.L. Visagie, C.J. Weststrate, J.W. Niemantsverdriet, Fischer-Tropsch Synthesis: Catalysts and Chemistry, in: *Comprehensive Inorganic Chemistry II*, Elsevier (2013) 525–557, <https://doi.org/10.1016/B978-0-08-097774-4.00729-4>.
- [10] Y. Cheng, M. Qiao, B. Zong, Fischer-Tropsch Synthesis, in: *Encyclopedia of Sustainable Technologies*, Elsevier, 2017: pp. 403–410. <https://doi.org/10.1016/B978-0-12-409548-9.10107-1>.
- [11] F. Lu, X. Chen, Z. Lei, L. Wen, Y. Zhang, Revealing the activity of different iron carbides for Fischer-Tropsch synthesis, *Appl Catal B* 281 (2021) 119521, <https://doi.org/10.1016/j.apcatb.2020.119521>.
- [12] K. Cheng, M. Virginie, V.V. Ordomsky, C. Cordier, P.A. Chernavskii, M.I. Ivantsov, S. Paul, Y. Wang, A.Y. Khodakov, Pore size effects in high-temperature Fischer-Tropsch synthesis over supported iron catalysts, *J. Catal.* 328 (2015) 139–150, <https://doi.org/10.1016/j.jcat.2014.12.007>.
- [13] M.J. Valero-Romero, M.Á. Rodríguez-Cano, J. Palomo, J. Rodríguez-Mirasol, T. Cordero, Carbon-Based Materials as Catalyst Supports for Fischer-Tropsch Synthesis: A Review, *Front. Mater.* 7 (2021), <https://doi.org/10.3389/fmats.2020.617432>.
- [14] Y. Suo, Y. Yao, Y. Zhang, S. Xing, Z.-Y. Yuan, Recent advances in cobalt-based Fischer-Tropsch synthesis catalysts, *J. Ind. Eng. Chem.* 115 (2022) 92–119, <https://doi.org/10.1016/j.jiec.2022.08.026>.
- [15] N.C. Shiba, X. Liu, Y. Yao, Advances in lower olefin production over cobalt-based catalysts via the Fischer-Tropsch process, *Fuel Process. Technol.* 238 (2022) 107489, <https://doi.org/10.1016/j.fuproc.2022.107489>.
- [16] K.-W. Jun, H.-S. Roh, K.-S. Kim, J.-S. Ryu, K.-W. Lee, Catalytic investigation for Fischer-Tropsch synthesis from bio-mass derived syngas, *Appl. Catal. A* 259 (2004) 221–226, <https://doi.org/10.1016/j.apcata.2003.09.034>.
- [17] A.Y. Khodakov, A. Griboval-Constant, R. Bechara, V.L. Zholobenko, Pore Size Effects in Fischer-Tropsch Synthesis over Cobalt-Supported Mesoporous Silicas, *J. Catal.* 206 (2002) 230–241, <https://doi.org/10.1006/jcat.2001.3496>.
- [18] H. Xiong, Y. Zhang, K. Liew, J. Li, Fischer-Tropsch synthesis: The role of pore size for Co/SBA-15 catalysts, *J. Mol. Catal. A Chem.* 295 (2008) 68–76, <https://doi.org/10.1016/j.molcata.2008.08.017>.
- [19] W. Chen, Z. Fan, X. Pan, X. Bao, Effect of Confinement in Carbon Nanotubes on the Activity of Fischer-Tropsch Iron Catalyst, *J. Am. Chem. Soc.* 130 (2008) 9414–9419, <https://doi.org/10.1021/ja8008192>.
- [20] G. Yu, B. Sun, Y. Pei, S. Xie, S. Yan, M. Qiao, K. Fan, X. Zhang, B. Zong, Fe_xO_y @C Spheres as an Excellent Catalyst for Fischer-Tropsch Synthesis, *J. Am. Chem. Soc.* 132 (2010) 935–937, <https://doi.org/10.1021/ja906370b>.
- [21] D. Uykun Mangaloğlu, M. Baranak, Ö. Ataç, H. Atakül, Effect of the promoter presence in catalysts on the compositions of Fischer-Tropsch synthesis products,

- J. Ind. Eng. Chem. 66 (2018) 298–310, <https://doi.org/10.1016/j.jiec.2018.05.044>.
- [22] Y. Yang, H.-W. Xiang, Y.-Y. Xu, L. Bai, Y.-W. Li, Effect of potassium promoter on precipitated iron-manganese catalyst for Fischer-Tropsch synthesis, Appl. Catal. A 266 (2004) 181–194, <https://doi.org/10.1016/j.apcata.2004.02.018>.
- [23] L. Niu, X. Liu, X. Wen, Y. Yang, J. Xu, Y. Li, Effect of potassium promoter on phase transformation during H₂ pretreatment of a Fe₂O₃ Fischer Tropsch synthesis catalyst precursor, Catal. Today 343 (2020) 101–111, <https://doi.org/10.1016/j.cattod.2019.01.054>.
- [24] Y. Yang, H. Zhang, H. Ma, W. Qian, Q. Sun, W. Ying, Effect of alkalis (Li, Na, and K) on precipitated iron-based catalysts for high-temperature Fischer-Tropsch synthesis, Fuel 326 (2022) 125090, <https://doi.org/10.1016/j.fuel.2022.125090>.
- [25] W. Zhou, K. Cheng, J. Kang, C. Zhou, V. Subramanian, Q. Zhang, Y. Wang, New horizon in C1 chemistry: breaking the selectivity limitation in transformation of syngas and hydrogenation of CO 2 into hydrocarbon chemicals and fuels, Chem. Soc. Rev. 48 (2019) 3193–3228, <https://doi.org/10.1039/C8CS00502H>.
- [26] S. Sartipi, M. Makkee, F. Kapteijn, J. Gascon, Catalysis engineering of bifunctional solids for the one-step synthesis of liquid fuels from syngas: a review, Catal. Sci. Technol. 4 (2014) 893–907, <https://doi.org/10.1039/C3CY01021J>.
- [27] Z. Wang, J. Yu, R. Xu, Needs and trends in rational synthesis of zeolitic materials, Chem. Soc. Rev. 41 (2012) 1729–1741, <https://doi.org/10.1039/C1CS15150A>.
- [28] K. Cheng, J. Kang, D.L. King, V. Subramanian, C. Zhou, Q. Zhang, Y. Wang, Advances in Catalysis for Syngas Conversion to Hydrocarbons, in: 2017: pp. 125–208. <https://doi.org/10.1016/bs.acat.2017.09.003>.
- [29] Y. Chen, J. Zhang, X. Jiang, L. Wei, Z. Li, C. Liu, Nano-ZSM-5 decorated cobalt based catalysts for Fischer-Tropsch synthesis to enhance the gasoline range products selectivity, J. Taiwan Inst. Chem. Eng. 116 (2020) 153–159, <https://doi.org/10.1016/j.jtice.2020.11.007>.
- [30] J. Plana-Pallejà, S. Abelló, C. Berruero, D. Montané, Effect of zeolite acidity and mesoporosity on the activity of Fischer-Tropsch Fe/ZSM-5 bifunctional catalysts, Appl. Catal. A 515 (2016) 126–135, <https://doi.org/10.1016/j.apcata.2016.02.004>.
- [31] X. Peng, K. Cheng, J. Kang, B. Gu, X. Yu, Q. Zhang, Y. Wang, Impact of Hydrogenolysis on the Selectivity of the Fischer-Tropsch Synthesis: Diesel Fuel Production over Mesoporous Zeolite-Y-Supported Cobalt Nanoparticles, Angew. Chem. Int. Ed. 54 (2015) 4553–4556, <https://doi.org/10.1002/anie.201411708>.
- [32] K. Cheng, L. Zhang, J. Kang, X. Peng, Q. Zhang, Y. Wang, Selective Transformation of Syngas into Gasoline-Range Hydrocarbons over Mesoporous H-ZSM-5-Supported Cobalt Nanoparticles, Chem. A Eur. J. 21 (2015) 1928–1937, <https://doi.org/10.1002/chem.201405277>.
- [33] P. Wang, J. Kang, Q. Zhang, Y. Wang, Lithium ion-exchanged zeolite faujasite as support of iron catalyst for Fischer-Tropsch synthesis, Catal Letters 114 (2007) 178–184, <https://doi.org/10.1007/s10562-007-9062-4>.
- [34] M. Baranak, B. Gürnlü, A. Saroğlu, Ö. Ataç, H. Atakül, Low acidity ZSM-5 supported iron catalysts for Fischer-Tropsch synthesis, Catal. Today 207 (2013) 57–64, <https://doi.org/10.1016/j.cattod.2012.04.013>.
- [35] N. Nikbakht, A.A. Mirzaei, H. Atashi, Kinetic modeling of the Fischer-Tropsch reaction over a zeolite supported Fe-Co-Ce catalyst prepared using impregnation procedure, Fuel 229 (2018) 209–216, <https://doi.org/10.1016/j.fuel.2018.04.132>.
- [36] F. Fazlollahi, M. Sarkari, H. Gharebaghi, H. Atashi, M.M. Zarei, A.A. Mirzaei, W. C. Hecker, Preparation of Fe-Mn/K/Al₂O₃ Fischer-Tropsch Catalyst and its Catalytic Kinetics for the Hydrogenation of Carbon Monoxide, Chin. J. Chem. Eng. 21 (2013) 507–519, [https://doi.org/10.1016/S1004-9541\(13\)60503-0](https://doi.org/10.1016/S1004-9541(13)60503-0).
- [37] J. Wei, Q. Ge, R. Yao, Z. Wen, C. Fang, L. Guo, H. Xu, J. Sun, Directly converting CO₂ into a gasoline fuel, Nat. Commun. 8 (2017) 15174, <https://doi.org/10.1038/ncomms15174>.
- [38] L. Shirazi, E. Jamshidi, M.R. Ghasemi, The effect of Si/Al ratio of ZSM-5 zeolite on its morphology, acidity and crystal size, Cryst. Res. Technol. 43 (2008) 1300–1306, <https://doi.org/10.1002/crat.200800149>.
- [39] N. Senamart, S. Buttha, W. Pantupho, I.Z. Koleva, S. Loiha, H.A. Aleksandrov, J. Wittayakun, G.N. Vayssilov, Characterization and temperature evolution of iron-containing species in HZSM-5 zeolite prepared from different iron sources, J. Porous Mater. 26 (2019) 1227–1240, <https://doi.org/10.1007/s10934-019-00718-w>.
- [40] M.K. Nieuwoudt, J.D. Comins, I. Cukrowski, The growth of the passive film on iron in 0.05 M NaOH studied *in situ* by Raman micro-spectroscopy and electrochemical polarisation. Part I: near-resonance enhancement of the Raman spectra of iron oxide and oxyhydroxide compounds, J. Raman Spectrosc. 42 (2011) 1335–1339, <https://doi.org/10.1002/jrs.2837>.
- [41] C.P. Marshall, W.J.B. Dufresne, C.J. Ruffledt, Polarized Raman spectra of hematite and assignment of external modes, J. Raman Spectrosc. 51 (2020) 1522–1529, <https://doi.org/10.1002/jrs.5824>.
- [42] R. Hu, T. Wang, Y. Wang, Y. Zhu, L. Xie, E. Xing, Y. Wu, Z. Da, Nano-Hollow Zeolite-Encapsulated Highly Dispersed Ultra-Fine Fe Nanoparticles as Fischer-Tropsch Catalyst for Syngas-to-Olefins, Catalysts 13 (2023) 948, <https://doi.org/10.3390/catal13060948>.
- [43] R. Liu, Z. Ma, J.D. Sears, M. Juneau, M.L. Neidig, M.D. Porosoff, Identifying correlations in Fischer-Tropsch synthesis and CO₂ hydrogenation over Fe-based ZSM-5 catalysts, J. CO₂ Util. 41 (2020) 101290, <https://doi.org/10.1016/j.jcou.2020.101290>.
- [44] W. Jiang, H.C. Yang, S.Y. Yang, H.E. Horng, J.C. Hung, Y.C. Chen, C.-Y. Hong, Preparation and properties of superparamagnetic nanoparticles with narrow size distribution and biocompatible, J. Magn. Magn. Mater. 283 (2004) 210–214, <https://doi.org/10.1016/j.jmmm.2004.05.022>.
- [45] Y. Xu, J. Wang, G. Ma, J. Bai, Y. Du, M. Ding, Direct synthesis of aromatics from syngas over Mo-modified Fe/HZSM-5 bifunctional catalyst, Appl. Catal. A 598 (2020) 117589, <https://doi.org/10.1016/j.apcata.2020.117589>.
- [46] H.H.P. Yiu, M.A. Keane, Z.A.D. Lethbridge, M.R. Lees, A.J. El Haj, J. Dobson, Synthesis of novel magnetic iron metal-silica (Fe-SBA-15) and magnetite-silica (Fe₃O₄-SBA-15) nanocomposites with a high iron content using temperature-programmed reduction, Nanotechnology 19 (2008) 255606, <https://doi.org/10.1088/0957-4484/19/25/255606>.
- [47] C.S. Stoicescu, D. Culita, N. Stanica, F. Papa, R.N. State, G. Munteanu, Temperature programmed reduction of a core-shell synthetic magnetite: Dependence on the heating rate of the reduction mechanism, Thermochim Acta 709 (2022) 179146, <https://doi.org/10.1016/j.tca.2022.179146>.
- [48] Q. Liu, Y. Fang, C. Miao, Z. Liao, J. Lu, J. Li, X. Wu, A. Nulalong, Preparation of ZSM-5 molecular sieve modified by kaolin and its CO₂ adsorption performance investigation, Microporous Mesoporous Mater. 360 (2023) 112678, <https://doi.org/10.1016/j.micromeso.2023.112678>.
- [49] Y. Xu, J. Liu, G. Ma, J. Wang, J. Lin, H. Wang, C. Zhang, M. Ding, Effect of iron loading on acidity and performance of Fe/HZSM-5 catalyst for direct synthesis of aromatics from syngas, Fuel 228 (2018) 1–9, <https://doi.org/10.1016/j.fuel.2018.04.151>.
- [50] H. Liu, Y. Fu, M. Li, J. Wang, A. Noreen, E. Maturura, X. Gao, R. Yang, C.C. Amoo, C. Xing, Activated carbon templated synthesis of hierarchical zeolite Y-encapsulated iron catalysts for enhanced gasoline selectivity in CO hydrogenation, J Mater Chem A Mater 9 (2021) 8663–8673, <https://doi.org/10.1039/D0TA12423K>.
- [51] W.Y. Mao, H.F. Ma, H.T. Zhang, Q.W. Sun, W.Y. Ying, D.Y. Fang, Links between Reaction Intermediates, Reactivity, and Reaction Conditions in Oxygenates Formation during Fischer-Tropsch Synthesis, Energy Sources Part A 36 (2014) 2175–2182, <https://doi.org/10.1080/15567036.2013.767864>.
- [52] L. Tian, C.-F. Huo, D.-B. Cao, Y. Yang, J. Xu, B.-S. Wu, H.-W. Xiang, Y.-Y. Xu, Y.-W. Li, Effects of reaction conditions on iron-catalyzed Fischer-Tropsch synthesis: A kinetic Monte Carlo study, J. Mol. Struct. (Theochem) 941 (2010) 30–35, <https://doi.org/10.1016/j.theochem.2009.10.032>.
- [53] E. de Smit, F. Cinquini, A.M. Beale, O.V. Safonova, W. van Beek, P. Sautet, B. M. Weckhuysen, Stability and Reactivity of ϵ - γ -0 Iron Carbide Catalyst Phases in Fischer-Tropsch Synthesis: Controlling μ C, J. Am. Chem. Soc. 132 (2010) 14928–14941, <https://doi.org/10.1021/ja105853q>.
- [54] A. Nakhaei Pour, M.R. Housaindokht, Fischer-Tropsch synthesis on iron catalyst promoted with HZSM-5 zeolite: Regeneration studies of catalyst, J. Nat. Gas Sci. Eng. 14 (2013) 49–54, <https://doi.org/10.1016/j.jngse.2013.05.004>.
- [55] S.A. Eliason, C.H. Bartholomew, Reaction and deactivation kinetics for Fischer-Tropsch synthesis on unpromoted and potassium-promoted iron catalysts, Appl. Catal. A 186 (1999) 229–243, [https://doi.org/10.1016/S0926-860X\(99\)00146-5](https://doi.org/10.1016/S0926-860X(99)00146-5).
- [56] W. Ning, N. Koizumi, H. Chang, T. Mochizuki, T. Itoh, M. Yamada, Phase transformation of unpromoted and promoted Fe catalysts and the formation of carbonaceous compounds during Fischer-Tropsch synthesis reaction, Appl. Catal. A 312 (2006) 35–44, <https://doi.org/10.1016/j.apcata.2006.06.025>.
- [57] F.G. Botes, The effect of a higher operating temperature on the Fischer-Tropsch/HZSM-5 bifunctional process, Appl. Catal. A 284 (2005) 21–29, <https://doi.org/10.1016/j.apcata.2005.01.012>.
- [58] Y.-Y. Ji, H.-W. Xiang, J.-L. Yang, Y.-Y. Xu, Y.-W. Li, B. Zhong, Effect of reaction conditions on the product distribution during Fischer-Tropsch synthesis over an industrial Fe-Mn catalyst, Appl. Catal. A 214 (2001) 77–86, [https://doi.org/10.1016/S0926-860X\(01\)00480-X](https://doi.org/10.1016/S0926-860X(01)00480-X).
- [59] B. Todici, L. Nowicki, N. Nikacevic, D.B. Bukur, Fischer-Tropsch synthesis product selectivity over an industrial iron-based catalyst: Effect of process conditions, Catal. Today 261 (2016) 28–39, <https://doi.org/10.1016/j.cattod.2015.09.005>.
- [60] J. Liu, Y. Song, X. Guo, C. Song, X. Guo, Recent advances in application of iron-based catalysts for CO hydrogenation to value-added hydrocarbons, Chin. J. Catal. 43 (2022) 731–754, [https://doi.org/10.1016/S1872-2067\(21\)63802-0](https://doi.org/10.1016/S1872-2067(21)63802-0).
- [61] Y. Liu, B.-T. Teng, X.-H. Guo, Y. Li, J. Chang, L. Tian, X. Hao, Y. Wang, H.-W. Xiang, Y.-Y. Xu, Y.-W. Li, Effect of reaction conditions on the catalytic performance of Fe-Mn catalyst for Fischer-Tropsch synthesis, J. Mol. Catal. A Chem. 272 (2007) 182–190, <https://doi.org/10.1016/j.molcata.2007.03.046>.
- [62] O. Akbarzadeh, N.A. Mohd Zabidi, G. Wang, A. Kordijazi, H. Sadabadi, S. Moosavi, A. Amani Babadi, N.A. Hamizi, Y. Abdul Wahab, M. Ab Rahman, S. Sagadevan, Z. Z. Chowdhury, M.R. Johan, Effect of Pressure, H₂/CO Ratio and Reduction Conditions on Co-Mn/CNT Bimetallic Catalyst Performance in Fischer-Tropsch Reaction, Symmetry (basel) 12 (2020) 698, <https://doi.org/10.3390/sym12050698>.
- [63] C. Niu, M. Xia, C. Chen, Z. Ma, L. Jia, B. Hou, D. Li, Effect of process conditions on the product distribution of Fischer-Tropsch synthesis over an industrial cobalt-based catalyst using a fixed-bed reactor, Appl. Catal. A 601 (2020) 117630, <https://doi.org/10.1016/j.apcata.2020.117630>.
- [64] V.A. de la Peña O'Shea, M.C. Alvarez-Galvan, J.M. Campos-Martin, J.L.G. Fierro, Strong dependence on pressure of the performance of a Co/SiO₂ catalyst in Fischer-Tropsch slurry reactor synthesis, Catal Letters 100 (2005) 105–116, <https://doi.org/10.1007/s10562-004-3096-7>.
- [65] F.G. Botes, J.W. Niemantsverdriet, J. Van De Loosdrecht, A comparison of cobalt and iron based slurry phase Fischer-Tropsch synthesis, Catal. Today 215 (2013) 112–120, <https://doi.org/10.1016/j.cattod.2013.01.013>.
- [66] F.G. Botes, B.B. Breman, Development and Testing of a New Macro Kinetic Expression for the Iron-Based Low-Temperature Fischer-Tropsch Reaction, Ind. Eng. Chem. Res. 45 (2006) 7415–7426, <https://doi.org/10.1021/ie060491h>.

- [67] U. Burgun, H.R. Zonouz, H. Okutan, H. Atakül, S. Senkan, A. Sarioglan, G., Gumuslu Gur, Effects of Rare Earth Metal Promotion over Zeolite-Supported Fe-Cu-Based Catalysts on the Light Olefin Production Performance in Fischer-Tropsch Synthesis, *ACS Omega* 8 (2023) 648–662, <https://doi.org/10.1021/acsomega.2c05795>.
- [68] D. Peña, L. Jensen, A. Cognigni, R. Myrstad, T. Neumayer, W. van Beek, M. Rønning, The Effect of Copper Loading on Iron Carbide Formation and Surface Species in Iron-Based Fischer-Tropsch Synthesis Catalysts, *ChemCatChem* 10 (2018) 1300–1312, <https://doi.org/10.1002/cctc.201701673>.
- [69] E. de Smit, B.M. Weckhuysen, The renaissance of iron-based Fischer-Tropsch synthesis: on the multifaceted catalyst deactivation behaviour, *Chem. Soc. Rev.* 37 (2008) 2758, <https://doi.org/10.1039/b805427d>.
- [70] K. Cheng et al., “Advances in Catalysis for Syngas Conversion to Hydrocarbons,” 2017, pp. 125–208. doi: 10.1016/bs.acat.2017.09.003.
- [71] Y. Zhang, et al., Operando Spectroscopic Study of Dynamic Structure of Iron Oxide Catalysts during CO₂ Hydrogenation, *ChemCatChem* 10 (6) (Mar. 2018) 1272–1276, <https://doi.org/10.1002/cctc.201701779>.
- [72] Y. Zhang, et al., The study of structure-performance relationship of iron catalyst during a full life cycle for CO₂ hydrogenation, *J. Catal.* 378 (Oct. 2019) 51–62, <https://doi.org/10.1016/j.jcat.2019.08.001>.
- [73] C. Ma, et al., θ -Fe₃C dominated Fe@C core-shell catalysts for Fischer-Tropsch synthesis: Roles of θ -Fe₃C and carbon shell, *J. Catal.* 393 (Jan. 2021) 238–246, <https://doi.org/10.1016/j.jcat.2020.11.033>.
- [74] G.P. van der Laan, Kinetics, selectivity and scale up of the Fischer-Tropsch synthesis, Rijksuniversiteit Groningen, 1999. <https://research.rug.nl/en/publications/kinetics-selectivity-and-scale-up-of-the-fischer-tropsch-synthese> (accessed September 10, 2023).
- [75] G.P. van der Laan, A.A.C.M. Beenackers, R. Krishna, Multicomponent reaction engineering model for Fe-catalyzed Fischer-Tropsch synthesis in commercial scale slurry bubble column reactors, *Chem. Eng. Sci.* 54 (1999) 5013–5019, [https://doi.org/10.1016/S0009-2509\(99\)00225-0](https://doi.org/10.1016/S0009-2509(99)00225-0).
- [76] S. Ledakowicz, H. Nettelhoff, R. Kokuun, W.D. Deckwer, Kinetics of the Fischer-Tropsch synthesis in the slurry phase on a potassium promoted iron catalyst, *Ind. Eng. Chem. Process Des. Dev.* 24 (1985) 1043–1049, <https://doi.org/10.1021/i200031a025>.
- [77] M.E. Dry, Advances in Fischer-Tropsch Chemistry, *Product r&d* 15 (1976) 282–286, <https://doi.org/10.1021/i360060a012>.
- [78] G.A. Huff, C.N. Satterfield, Intrinsic kinetics of the Fischer-Tropsch synthesis on a reduced fused-magnetite catalyst, *Ind. Eng. Chem. Process Des. Dev.* 23 (1984) 696–705, <https://doi.org/10.1021/i200027a012>.
- [79] M. Ojeda, R. Nabar, A.U. Nilekar, A. Ishikawa, M. Mavrikakis, E. Iglesia, CO activation pathways and the mechanism of Fischer-Tropsch synthesis, *J. Catal.* 272 (2010) 287–297, <https://doi.org/10.1016/j.jcat.2010.04.012>.
- [80] L.-P. Zhou, X. Hao, J.-H. Gao, Y. Yang, B.-S. Wu, J. Xu, Y.-Y. Xu, Y.-W. Li, Studies and Discriminations of the Kinetic Models for the Iron-Based Fischer-Tropsch Catalytic Reaction in a Recycle Slurry Reactor, *Energy Fuel* 25 (2011) 52–59, <https://doi.org/10.1021/ef101270u>.
- [81] F.G. Botes, The Effects of Water and CO₂ on the Reaction Kinetics in the Iron-Based Low-Temperature Fischer-Tropsch Synthesis: A Literature Review, *Catal. Rev.* 50 (2008) 471–491, <https://doi.org/10.1080/01614940802477250>.
- [82] M. Schmal, *Catálise Heterogênea*, 1st ed., Synergia Editora, Rio de Janeiro, 2012 <https://www.livrariasynergia.com.br/livros/S18526/9788561325534/catalise-heterogenea.html>.
- [83] M. Dry, Rate of the Fischer-Tropsch reaction over iron catalysts, *J. Catal.* 25 (1972) 99–104, [https://doi.org/10.1016/0021-9517\(72\)90205-9](https://doi.org/10.1016/0021-9517(72)90205-9).
- [84] J. Santos, L. Bobadilla, M. Centeno, J. Odriozola, Operando DRIFTS-MS Study of WGS and rWGS Reaction on Biochar-Based Pt Catalysts: The Promotional Effect of Na, *C (basel)* 4 (2018) 47, <https://doi.org/10.3390/c4030047>.
- [85] A. Eshraghi, A.A. Mirzaei, H. Atashi, Kinetics of the Fischer-Tropsch reaction in fixed-bed reactor over a nano-structured Fe-Co-Ce catalyst supported with SiO₂, *J. Nat. Gas Sci. Eng.* 26 (2015) 940–947, <https://doi.org/10.1016/j.jngse.2015.06.036>.
- [86] M. Polisi, J. Grand, R. Arletti, N. Barrier, S. Komaty, M. Zaarour, S. Mintova, G. Vezzalini, CO₂ Adsorption/Desorption in FAU Zeolite Nanocrystals, In Situ Synchrotron X-Ray Powder Diffraction and in Situ Fourier Transform Infrared Spectroscopic Study, the *Journal of Physical Chemistry C* 123 (2019) 2361–2369, <https://doi.org/10.1021/acs.jpcc.8b11811>.
- [87] M. Kollár, A. De Stefanis, H.E. Solt, M.R. Mihályi, J. Vályon, A.A.G. Tomlinson, The mechanism of the Fischer-Tropsch reaction over supported cobalt catalysts, *J. Mol. Catal. A Chem.* 333 (2010) 37–45, <https://doi.org/10.1016/j.molcata.2010.09.014>.
- [88] J. Weiß, Q. Yang, U. Bentrup, E.V. Kondratenko, A. Brückner, C. Kubis, Operando DRIFT and In situ Raman Spectroscopic Studies on Aspects of CO₂ Fischer-Tropsch Synthesis Catalyzed by Bulk Iron Oxide-Based Catalysts, *ChemCatChem* 14 (2022), <https://doi.org/10.1002/cctc.202200577>.